SANDIA REPORT

SAND2009-6424
Unlimited Release
Printed September 2009

Room Temperature Synthesis of Ni-based Alloy Nanoparticles by Radiolysis

Tina M. Nenoff, Zhenyuan Zhang, Kevin Leung, Roland Stumpf, Jianyu Huang, Ping Lu, Donald T. Berry, Paula P. Provencio, Donald Hanson, David Robinson, Benjamin Jacobs

Prepared by
Sandia National Laboratories
Albuquerque, New Mexico 87185 and Livermore, California 94550

Sandia is a multiprogram laboratory operated by Sandia Corporation,
a Lockheed Martin Company, for the United States Department of Energy's
National Nuclear Security Administration under Contract DE-AC04-94AL85000.

Sandia National Laboratories

Issued by Sandia National Laboratories, operated for the United States Department of Energy by Sandia Corporation.

Printed in the United States of America. This report has been reproduced directly from the best available copy.

Available to DOE and DOE contractors from
U.S. Department of Energy
Office of Scientific and Technical Information
P.O. Box 62
Oak Ridge, TN 37831

Telephone: (865) 576-8401
Facsimile: (865) 576-5728
E-Mail: reports@adonis.osti.gov
Online ordering: http://www.osti.gov/bridge

Available to the public from
U.S. Department of Commerce
National Technical Information Service
5285 Port Royal Rd.
Springfield, VA 22161

Telephone: (800) 553-6847
Facsimile: (703) 605-6900
E-Mail: orders@ntis.fedworld.gov
Online order: http://www.ntis.gov/help/ordermethods.asp?loc=7-4-0#online

SAND2009-6424
Unlimited Release
Printed September 2009

Room Temperature Synthesis of Ni-based Alloy Nanoparticles by Radiolysis

Tina M. Nenoff, Zhenyuan Zhang, Kevin Leung, Roland Stumpf, Jianyu Huang, Ping Lu,
Donald T. Berry, Paula P. Provencio
Sandia National Laboratories
P.O. Box 5800
Albuquerque, New Mexico 87185

Abstract

Room temperature radiolysis, density functional theory, and various nanoscale characterization methods were used to synthesize and fully describe Ni-based alloy nanoparticles (NPs) that were synthesized at room temperature. These complementary methods provide a strong basis in understanding and describing metastable phase regimes of alloy NPs whose reaction formation is determined by kinetic rather than thermodynamic reaction processes. Four series of NPs, (Ag-Ni, Pd-Ni, Co-Ni, and W-Ni) were analyzed and characterized by a variety of methods, including UV-vis, TEM/HRTEM, HAADF-STEM and EFTEM mapping.

In the first focus of research, AgNi and PdNi were studied. Different ratios of Ag_x- Ni_{1-x} alloy NPs and $Pd_{0.5}$- $Ni_{0.5}$ alloy NP were prepared using a high dose rate from gamma irradiation. Images from high-angle annular dark-field (HAADF) show that the Ag-Ni NPs are not core-shell structure but are homogeneous alloys in composition. Energy filtered transmission electron microscopy (EFTEM) maps show the homogeneity of the metals in each alloy NP. Of particular interest are the normally immiscible Ag-Ni NPs. All evidence confirmed that homogeneous Ag-Ni and Pd-Ni alloy NPs presented here were successfully synthesized by high dose rate radiolytic methodology. A mechanism is provided to explain the homogeneous formation of the alloy NPs. Furthermore, studies of Pd-Ni NPs by in situ TEM (with heated stage) shows the ability to sinter these NPs at temperatures below 800°C.

In the second set of work, CoNi and WNi superalloy NPs were attempted at 50/50 concentration ratios using high dose rates from gamma irradiation. Preliminary results on synthesis and characterization have been completed and are presented. As with the earlier alloy NPs, no evidence of core-shell NP formation occurs. Microscopy results seem to indicate alloying occurred with the CoNi alloys. However, there appears to be incomplete reduction of the Na_2WO_4 to form the W^{2+} ion in solution; the predominance of WO^+ appears to have resulted in a W-O-Ni complex that has not yet been fully characterized.

ACKNOWLEDGEMENTS

This work was supported in part by the Laboratory Directed Research and Development (LDRD) program of Sandia National Laboratories. Sandia National Laboratories is a multiprogram laboratory operated by Sandia Corporation, a Lockheed Martin Company, for the United States Department of Energy's National Nuclear Security Administration under contract DE-AC04-94AL85000.

TABLE OF CONTENTS

1. Introduction

Ni-based bimetallic bulk alloys are of great interest for a diverse range of applications including superalloys for aircraft and engine components,[1] shape memory materials for civil structures,[2] biomedical devices,[3] and hydrogen dissociative membranes.[4] Generally, these alloys are synthesized at elevated temperatures as melts. However, there is interest in developing lower temperature synthetic routes as a means of making more defect-free bulk alloys. One method for lower defects is the process of making high surface area nanoparticles (NPs) whose sintering temperature to bulk is predicted to be at a much lower temperature than the melt.[5] The overall process method is only helpful if the NPs are synthesized at low temperatures via kinetic formation processes. Therefore, we undertook a search for a potentially universal low temperature method of synthesizing NP alloys, independent of the thermodynamically most favored phases.

There is also great interest in Ni-based nanoparticles (NPs) for their technologically important catalytic and magnetic properties.[6-10] Recent reports describe various methods of synthesizing Ni-based bimetallic NPs. Most of the methods are at elevated temperatures such as thermal decomposition of transition metal complexes,[11-14] reverse micelles,[15, 16] chemical reduction,[17, 18] electrochemical formation,[19, 20] molecular beams,[21] ion implantation,[22] and sonochemical synthesis.[23] Recently, we and others have been utilizing room temperature radiolysis for NP formation.[24, 25] Gamma (γ)-radiation is a unique technique to prepare metallic NPs and has been found to be highly advantageous as compared to conventional chemical and photochemical methods.[26] These advantages include: (1) a controlled reduction of metal ions without using an excess of reducing agent or producing undesired oxidation products from the reductant, (2) a well-known rate of reaction, because the number of reducing equivalents generated by radiation is well defined, (3) radiation is absorbed without interference from light-absorbing solutes and products, and (4) the reducing agent is uniformly formed in the solution.[26]

The properties of Ni-based bimetallic NPs are greatly affected by the structures of NPs. In most cases, core-shell and alloy are the two most commonly used terms to describe the structure of bimetallic NPs. For example, Pd-Ni alloy NPs,[10] Pd core-Ni shell,[27] Ni core-Pd shell[28] NPs have been synthesized and the structures have been characterized and confirmed by X-ray diffraction (XRD), X-ray photoelectron spectroscopy (XPS), and extended X-ray absorption fine structure (EXAFS). However, it is very difficult to synthesize Ag-Ni alloy NPs because of the pronounced lattice mismatch, lower surface energy of Ag, and importantly, the complete immiscibility between Ag and Ni.[29] Therefore, it has been confirmed that phase segregated core-shell structure is the most thermodynamically stable structure for Ag-Ni NPs and Ag surface segregation from the Ni core.[29-31] Metastable Ag-Ni alloy NPs can be synthesized via laser-liquid-solid interaction technique[32, 33] and 25 nm crystalline Ag-Ni alloy NPs can be formed by stepwise reduction of Ag^+ and Ni^{2+}.[34] However, these methods either create Ag-rich and Ni-NiO-rich phases[32, 33] or a mixture of Ag-Ni, Ag, and Ni NPs[34] and a dealloying process of the Ag-Ni NPs may occur.[34] The difficulty associated with alloy Ag-Ni NPs formation was also supported by simulations and calculation from theory. All such theory modeling efforts, such as DFT, global optimization, molecular dynamics, and Monte Carlo simulations, showed that Ni core-Ag shell structures are thermodynamically favorable.[35-40]

I. AgNi and PdNi Nanoparticles

In this report, we demonstrate that different stoichiometries of Ag-Ni alloy NPs and $Pd_{0.5}$-$Ni_{0.5}$ alloy NPs can be prepared. Our work incorporates room temperature radiolysis reactions and various nanoscale characterization methods to fully characterize the Ag_x-Ni_{1-x} and $Pd_{0.5}$-$Ni_{0.5}$ alloy NPs. Utilizing first principles Density Functional Theory (DFT), we identify and confirm the NP formations via kinetic versus thermodynamic reaction pathways. We are able to correlate our experimental and characterization data with the modeling data to more fully describe the reaction pathways for these NPs and for potentially other NP compositional formations found in metastable phase regimes only accessible by radiolysis.

Experimental and computational methods

Synthesis

We have used a combination of room temperature synthesis, characterization, and first principles modeling to explore metastable phase spaces of various Ni-based alloy NP formations. In the synthesis, different stoichiometries of Ag-Ni NPs were prepared using the following radiolytic methodology; a 50 mL aqueous solution containing 0 to 2×10^{-4} M $AgClO_4$, 2 to 0 $\times 10^{-4}$ M $NiSO_4$, 3×10^{-4} M sodium citrate, 0.5 M methanol, and 1.5×10^{-2} M poly-vinyl alcohol (PVA, M_w, 88,000) were deaerated by bubbling Ar for 12 mins, and then irradiated in a ^{60}Co-γ source (Sandia National Laboratories Gamma Irradiation Facility (GIF)) at a dose rate of 300 rad/s for 18 mins. This corresponds to approximately four to seven times the dose required for total reduction of Ag^+ and Ni^{2+}, depending on the total concentration of metal ions from Ag^+ and Ni^{2+}. The total concentration of different stoichiometries of Ag^+ and Ni^{2+} was kept at 2×10^{-4} M (see Table 1). Similarly, for the $Pd_{0.5}$-$Ni_{0.5}$ (50% Pd and 50% Ni) alloy NPs preparation, a 50 mL aqueous solution containing 1×10^{-4} M $Pd(NH_3)_4Cl_2$, 1×10^{-4} M $NiSO_4$, 3×10^{-4} M sodium citrate, 0.5 M methanol, and 1.5×10^{-2} M poly-vinyl alcohol (PVA, M_w, 88,000) was irradiated at a dose rate of 300 rad/s for 36 min.

Table 1 Different stoichiometry of Ag^+ and Ni^{2+} used to prepare Ag-Ni alloy NPs

	Ag	$Ag_{0.9}$-$Ni_{0.1}$	$Ag_{0.7}$-$Ni_{0.3}$	$Ag_{0.5}$-$Ni_{0.5}$	$Ag_{0.3}$-$Ni_{0.7}$	Ni
$[Ag^+]$, $\times 10^{-4}$ M	2	1.8	1.4	1	0.6	0
$[Ni^{2+}]$, $\times 10^{-4}$ M	0	0.2	0.6	1	1.4	2
$[Ag^+] + [Ni^{2+}]$, $\times 10^{-4}$ M	2	2	2	2	2	2
$[Ag^+]:[Ni^{2+}]$	pure Ag NPs	9:1	7:3	1:1	3:7	pure Ni NPs

The reaction was carried out in a 100 mL vessel which was equipped with a sidearm containing a 0.5 cm optical path, and was sealed with two septa. This allowed for the collection of UV-vis spectra without exposing the solution to air. Full reduction of the metal ions was determined when there was no change in UV-vis spectra upon additional irradiation. Specimens for TEM were prepared by dropping the solution on a titanium-carbon grid and subsequent drying under N_2 gas in a glovebox. To examine whether Ag-Ni NPs were stable to dealloying, TEM grids with NPs were heated at 125 ºC for 6 hr and at 100 ºC for 9 hr in a vacuum oven.

Characterization

UV-vis absorption spectra were taken on a Varian Cary 300 Scan UV-Visible Spectrophotometer. Mean particle diameters, particle size distribution, and morphology were determined by using a JEOL 1200EX (120 kV) bright-field transmission electron microscopy (TEM) with Gatan digital imaging. High-resolution TEM and scanning TEM (STEM) images were acquired using an FEI Tecnai G(2) F30 S-Twin (300 kV) TEM at the Center for Integrated Nanotechnologies at Sandia National Laboratories (SNL CINT). This instrument is equipped with Z-contrast capability (to image different elements) with a resolution of 0.14 nm in high-angle annular dark-field (HAADF) mode. The unit is also equipped with energy-dispersive X-ray (EDX) analysis for detection of characteristic X-rays for elemental analysis, and with an electron energy-loss spectrometer (EELS) for characterizing composition and energy-filtered imaging. The VG HB501 Scanning Transmission Electron Microscope (STEM) and the TEAM microscope with an aberration corrector were operated at the National Center for Electron Microscopy at Lawrence Berkeley National Laboratory (LBNL). The unit is equipped with an Enfina parallel EELS detector for chemical analysis (energy resolution of 0.4eV) and a High Annular Dark Field Detector of Z-contrast image (atomic resolution of 0.1nm).

DFT Modeling

Spin-polarized DFT calculations were performed using the VASP code,[41, 42] the Perdew-Burke-Ernzerhof (PBE) exchange-correlation functional,[43] Γ-point Brillouin sampling, a 400 eV plane wave energy cutoff, and a 0.1 meV energy convergence criterion at each configuration. For Ag-Ni, the face-centered cubic (FCC) simulation cell of lattice constant 16 or 18 Å contained a single NP model of 240 atoms – 120 Ag/Pd and Ni each. The NP structure originated from an unrelaxed bulk FCC Ag metal lattice. A spherical nanoparticle of radius 10.8 Å centered in a tetrahedral void site was carved out, and the surface atoms were trimmed to create a core-single shell NP with a C_{3v} symmetry and all 120 Ag on the surface, where a "surface atom" is defined as having at most 9 nearest neighbors. The starting configuration of the Ag core-Ni shell NP was obtained by switching Ag and Ni atoms (analog for Pd-Ni). Two alloy NPs were created using random numbers to assign atom identities in the NP. This 50/50 composition allowed a direct comparison of the energetics of the two core-shell configurations as well as the random alloys, while a 240-atom NP is large enough that at least half the atoms can be considered residing in the interior. Conjugate gradient techniques were applied to relax the NP to local minima on the potential energy surfaces. Due to its massive reconstruction, the Ni core-Ag shell NP took more than 1000 steps to relax, while for other NPs, at most a few hundred steps is sufficient. The root-mean-squared remaining forces were 5.5, 14, 11, and 7.8 meV/Å, respectively, for the four clusters.

For Pd-Ni, the 240 atom FCC simulation cell consists of 120 Ni atoms and 120 Pd atoms. The atoms were allowed to relax to their local minimum energy geometry until all atomic force components were below 0.015 eV/Å. Eight different ordering of clusters were tested, including Ni core-Pd shell, Pd core-Ni shell, 4 different random alloys, and 2 different ordered alloys. The reference energy for the alloy cluster was determined by the sum of 120 Ni atoms in the pure 240 Ni atom cluster and 120 Pd atomic energies in the pure 240 Pd atom cluster. The reference energy for core-shell configurations is the energy per bulk Ni and Pd atom, corrected by the surface energy.[44]

Results and Discussion

The two series of NPs, Ag-Ni and Pd-Ni, were analyzed and characterized by a variety of methods, including UV-vis, TEM/HRTEM, HAADF-STEM and EFTEM mapping. The characterization methods allowed us to fully explore these room temperature metastable phase spaces.

Ag-Ni nanoparticles

Ag-Ni alloy NPs with varying stoichiometries (see Table 1) were prepared under similar reaction conditions (e. g. same total metal concentrations, same concentrations of stabilizers, and same irradiation time) and their UV-vis spectra are shown in Fig. 1. The plasmon peak of 90% Ag and 10% Ni ($Ag_{0.9}$-$Ni_{0.1}$, curve a) NPs is around 391 nm, similar to pure Ag NPs synthesized in the same condition. The plasmon peaks of 70% Ag and 30% Ni ($Ag_{0.7}$-$Ni_{0.3}$, curve b), 50% Ag and 50% Ni ($Ag_{0.5}$-$Ni_{0.5}$, curve c), and 30% Ag and 70% Ni ($Ag_{0.3}$-$Ni_{0.7}$, curve d) NPs are all around 383 nm. Comparing all the curves, the relative intensity of the plasmon peak is decreased as Ni concentration is increased. The absorption spectrum for pure Ni NPs has a very weak peak around 330 nm according to Mie theoretic calculations[45] and most literature reports show no absorption band for Ni NPs. However, the presence of Ni can dampen the Ag plasmon band and shift it blue.[29, 30] Therefore, $Ag_{0.9}$-$Ni_{0.1}$ NPs have the highest intensity of Ag plasmon band and $Ag_{0.3}$-$Ni_{0.7}$ have the lowest. The UV-vis spectra in Fig. 1 indeed indicate different concentrations of Ag in different stoichiometries of Ag-Ni NPs.

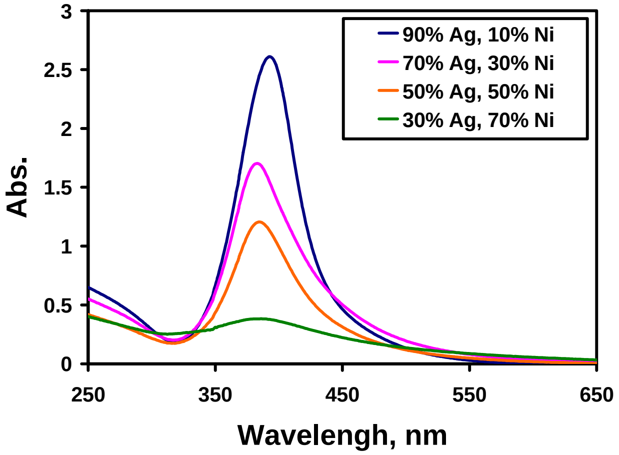

Figure 1. UV-vis spectra of Ag-Ni alloy NPs as-synthesized after 18 min irradiation (full reduction). The spectra are from Ag-Ni alloy NPs of 90% Ag, 10% Ni ($Ag_{0.9}$-$Ni_{0.1}$, curve a), 70% Ag, 30% Ni ($Ag_{0.7}$-$Ni_{0.3}$, curve b), 50% Ag, 50% Ni ($Ag_{0.5}$-$Ni_{0.5}$, curve c), and 30% Ag, 70% Ni ($Ag_{0.3}$-$Ni_{0.7}$, curve d). Absorbance is normalized to 1 cm optical path.

Reaction conditions also had an effect on particle size and shape. PVA and citrate ions offer good steric isolation and stability between individual NPs. Due to the reaction solution containing both stabilizers, the as-synthesized NPs are spherical in shape (Fig. 2). Table 2 lists the particle size in diameter and size distribution of as-synthesized Ag, Ag-Ni, and Ni NPs and Fig. 2 shows the TEM images of as-synthesized NPs. From the data in Fig. 2 and Table 2, it is clear that the particle size becomes smaller as the Ni percentage increases within the NPs.

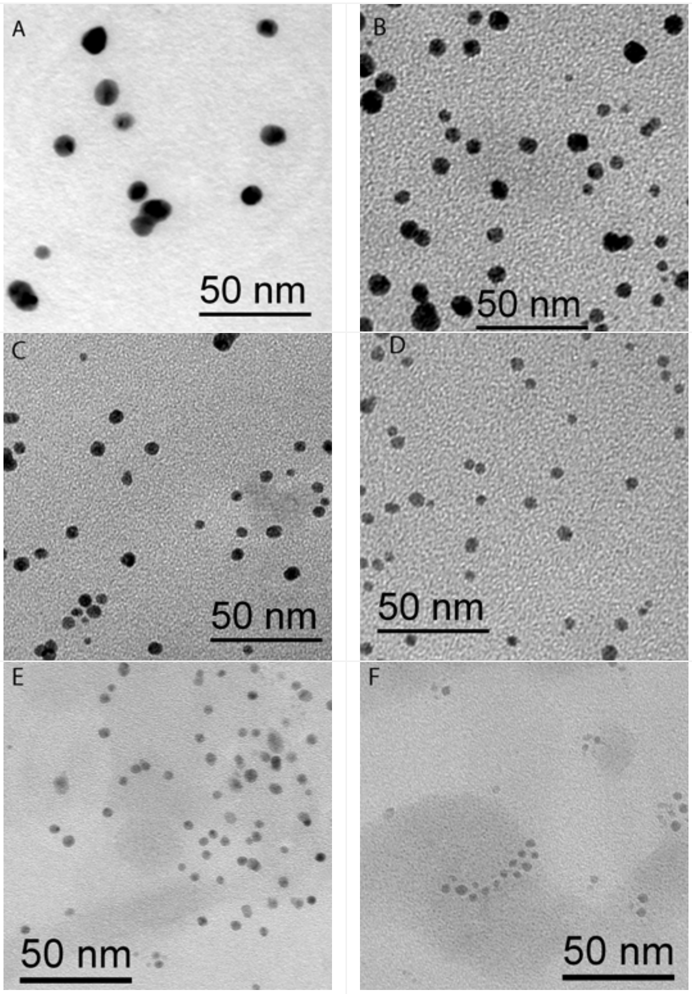

Figure 2. TEM image of Ag, Ag-Ni, and Ni NPs as-synthesized (A) pure Ag NPs (B) $Ag_{0.9}$-$Ni_{0.1}$ (C) $Ag_{0.7}$-$Ni_{0.3}$ (D) $Ag_{0.5}$-$Ni_{0.5}$[a] (E) $Ag_{0.3}$-$Ni_{0.7}$ (F) pure Ni NPs. All scale bars are 50 nm. [a]Sample from reference 25.

Table 2 Particle size in diameter and size distribution of Ag, Ag-Ni, and Ni NPs

	Ag	$Ag_{0.9}$-$Ni_{0.1}$	$Ag_{0.7}$-$Ni_{0.3}$	$Ag_{0.5}$-$Ni_{0.5}$	$Ag_{0.3}$-$Ni_{0.7}$	Ni
size in diameter, nm	8.5	7.4	5.7	5.4	4.0	3.4
size distribution	24%	24%	20%	15%	18%	19%

Aging of the NPs consistently has an effect on the NPs size.[25] In the Ag-Ni series, a damping and red shift of the band in UV-vis spectra is seen with up to 6 days of aging. After 6 days there is no change in the spectra, indicating no change in particle size. The damping and shift may be caused by a ripening process as there is a slight increase in particle size TEM or HRTEM can be used to distinguish the presence of alloy versus core-shell NP structures. Several groups have reported TEM images that clearly show core-shell structures of various bimetallic NPs.[46-48] In previously published work, our TEM results also showed the clear core-shell image of 8 nm Pt NPs coated with Ag shell.[25] Ferrer et al. demonstrated clear Au core-Pd shell NPs in HRTEM.[46] In contrast, HRTEM results of $\mathrm{Ag}_{0.5}$-$\mathrm{Ni}_{0.5}$[25] and the other Ag-Ni NPs presented here show metal alloy lattice patterns (with no evidence of Ag and Ni contrast in the images). In this current work, we note that a few of the pure Ag and Ag-Ni NPs have some shading on the NPs as viewed by TEM (see fig 2). This is due to the different particle surface morphology and orientations. These images do not indicate a core-shell structure. Neither our TEM nor HRTEM images show core-shell structure in the Ag-Ni NPs. This is confirmed by our subsequent detailed analyses (see below).

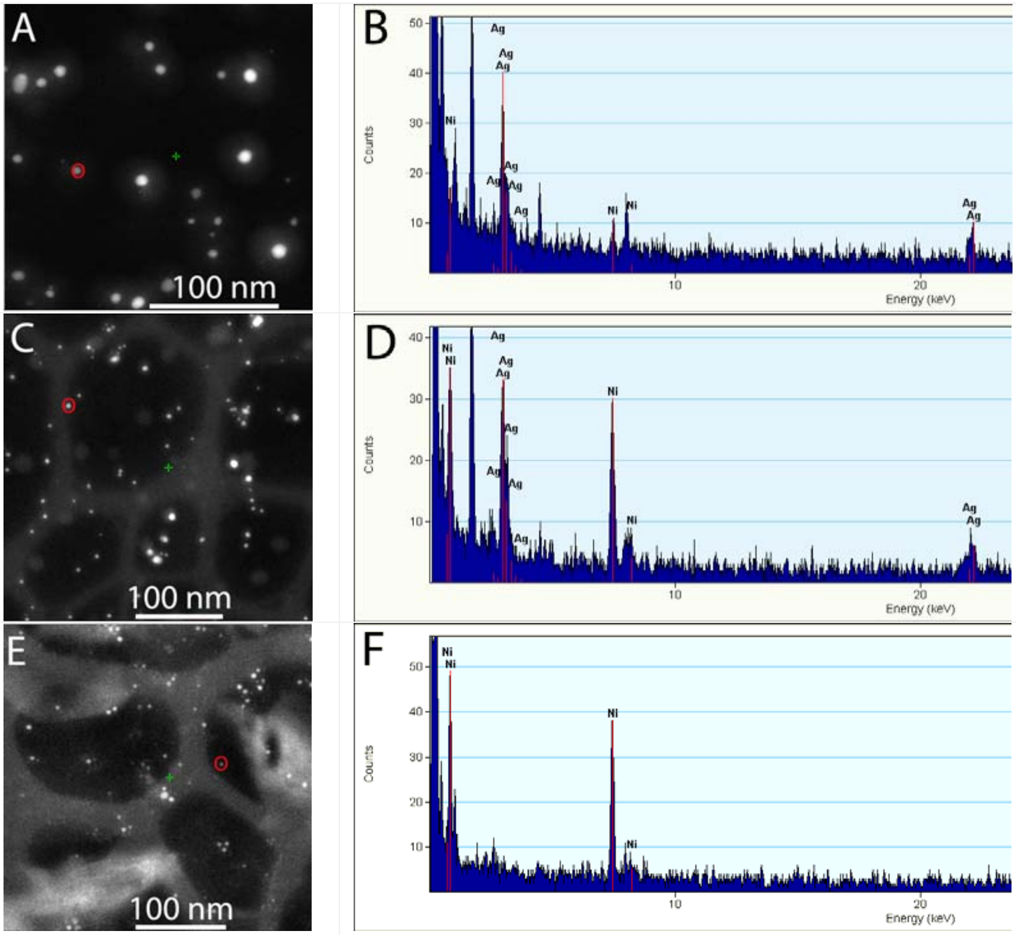

Figure 3. HAADF-STEM image of $\mathrm{Ag}_{0.7}$-$\mathrm{Ni}_{0.3}$ (A), $\mathrm{Ag}_{0.3}$-$\mathrm{Ni}_{0.7}$ (C), and pure Ni NPs (E). Scale bars: 100 nm. Single particle EDX of $\mathrm{Ag}_{0.7}$-$\mathrm{Ni}_{0.3}$ (B), $\mathrm{Ag}_{0.3}$-$\mathrm{Ni}_{0.7}$ (D), and pure Ni NPs (F). The single particle EDX analysis is from a particle as indicated by a red circle in (A), (C), and (E). The EDX analysis shows the peaks from both Ag and Ni for $\mathrm{Ag}_{0.7}$-$\mathrm{Ni}_{0.3}$ (B) and $\mathrm{Ag}_{0.3}$-$\mathrm{Ni}_{0.7}$ (D) NPs and thus indicates the presence of both elements in one particle for these NPs.

High-angle annular dark-field scanning-transmission electron microscopy (HAADF-STEM) was used as a powerful technique to visualize structural and chemical information of the nanoscale NPs. The intensity of HAADF images is approximately proportional to $Z^{1.7}$ (Z, atomic number).[46, 49] Because the intensity difference from atomic numbers (Z) of bimetallic Ag-Ni and Pd-Ni NPs can give a clear contrast in HAADF images, the presence or absence of a core-shell structure of bimetallic NPs can be confirmed from this kind of Z-contrast imaging. For example, Jose-Yacaman et al. showed that Pd core-Au shell NPs gave a clear contrast in the HAADF image.[46] HAADF-STEM images were collected from our $Ag_{0.7}$-$Ni_{0.3}$, $Ag_{0.3}$-$Ni_{0.7}$, and Ni NPs, respectively (see Fig. 3). It is very clear that there are no core-shell structures in $Ag_{0.7}$-$Ni_{0.3}$ and $Ag_{0.3}$-$Ni_{0.7}$ NPs. Both sets of images are very similar to the image of pure Ni NPs in Figure 3E. This evidence indicates that Ag and Ni are homogeneously distributed throughout each $Ag_{0.7}$-$Ni_{0.3}$ and $Ag_{0.3}$-$Ni_{0.7}$ NP.

A single NP shown in Fig. 3A was analyzed by EDX; the analysis shows clearly the presence of both Ag and Ni in one single $Ag_{0.7}$-$Ni_{0.3}$ NP, albeit with some noise. The single particle EDX of $Ag_{0.3}$-$Ni_{0.7}$ in Fig. 3C shows strong peaks from both Ag and Ni with less noise because of the high percentage of Ni in $Ag_{0.3}$-$Ni_{0.7}$ NPs. In fact, the intensity of the Ni peak in Fig. 3C is very similar to that of a pure single Ni NP from Fig. 3E. Our attempts to detect Ni in $Ag_{0.9}$-$Ni_{0.1}$ NPs from single particle EDX were not successful. It is probably below the detection limit of the machine due to the low Ni percentage in $Ag_{0.9}$-$Ni_{0.1}$ NP. The presence of Ni is further confirmed in each nanoparticle by the AgNi NP EFTEM mapping studies which clearly show that both Ni and Ag are present within one single particle and that both elements are homogeneously distributed in each NP (see below).

As shown in Fig. 1, the consistent trends in the UV-vis results indicate that Ag percentage decreases from $Ag_{0.9}$-$Ni_{0.1}$ to $Ag_{0.3}$-$Ni_{0.7}$ as shown by the intensity decrease from Ag plasmon band. The exact stoichiometry of each individual NP in single particle EDX in Fig. 3 was analyzed by the EDX analysis software (Table 3). Though there is substantial noise in each data set, due to the small size of the NPs, an approximate value can be determined per NP. The largest error in EDX is for $Ag_{0.7}$-$Ni_{0.3}$ in Fig. 3B due to the EDX spectra having a large signal to noise ratio. The analysis shows that there is 56% Ni and 44% Ag in one single $Ag_{0.5}$-$Ni_{0.5}$ NP and 57% Ni and 43% Ag in one $Ag_{0.3}$-$Ni_{0.7}$ NP (Table 3).

Table 3 EDX quantitative analysis of single Ag_x-Ni_{1-x} NP.

	$Ag_{0.7}$-$Ni_{0.3}$	$Ag_{0.5}$-$Ni_{0.5}$[a]	$Ag_{0.3}$-$Ni_{0.7}$
ratios from preparation	70% Ag, 30% Ni	50% Ag, 50% Ni	30% Ag, 70% Ni
ratios from EDX analysis	91% Ag, 8.6% Ni	44% Ag, 56% Ni[a]	43% Ag, 57% Ni

[a] Component analysis is from Fig. 3B in reference 25.

Elemental mapping by energy filtered transmission electron microscopy (EFTEM) provides information on particle chemical uniformity and topochemistry, and distribution of chemical components with high spatial resolution.[50] This elemental map can be characteristic for particular elements, and therefore, the elemental distribution images can be recorded with atomic or nanometer resolution.[50, 51] Fig. 4 shows the carbon, Ni, Ag maps, and zero loss image of our $Ag_{0.9}$-$Ni_{0.1}$ NPs. The spatial distribution of all the bright spots from the elemental maps of Ni and Ag is consistent with that in the zero loss image. The carbon map shows that the background of the NPs, where the amorphous carbon is present on TEM grid, is bright, while the NPs are dark. The spatial distribution of NPs in the carbon map is also consistent with that found in the Ni and Ag maps. The Ni and Ag maps indicate that both Ag and Ni are present in the $Ag_{0.9}$-$Ni_{0.1}$ alloy NPs. Importantly, the shape of bright spots from both Ni and Ag maps, as well as that from zero loss image, is the same. This implies that Ni and Ag are uniformly distributed in each individual nanoparticle.

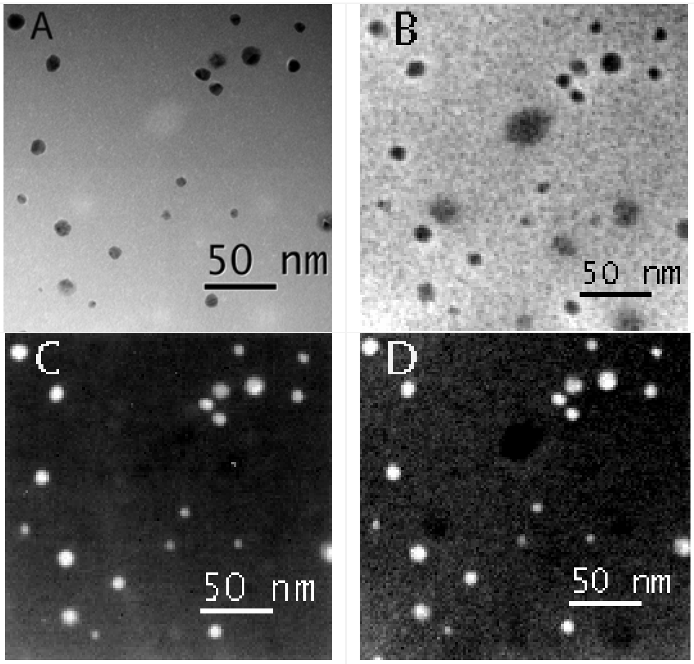

Figure 4. EFTEM maps of $Ag_{0.9}$-$Ni_{0.1}$ NPs. (A) zero loss image, (B) carbon map, (C) Ni map, and (D) Ag map. All scale bars are 50 nm.

The EFTEM maps for the $Ag_{0.7}$-$Ni_{0.3}$ NPs samples are shown in Fig. 5. The results are similar to the previously described sample of $Ag_{0.9}$-$Ni_{0.1}$ in Fig. 4 and demonstrate that both Ni and Ag are present. The spatial distribution of $Ag_{0.7}$-$Ni_{0.3}$ NPs in both images is also consistent. The spatial distribution of Ni and Ag maps of $Ag_{0.7}$-$Ni_{0.3}$ NPs is also consistent with the zero loss image. EFTEM map results from $Ag_{0.3}$-$Ni_{0.7}$ in Fig. 5 also show that Ni and Ag are uniformly distributed within the whole particle. The EFTEM map results from both $Ag_{0.7}$-$Ni_{0.3}$ and $Ag_{0.3}$-$Ni_{0.7}$ NPs further confirmed the homogeneity of alloy structure in these NPs. Our HRTEM, HAADF-STEM, and EFTEM map results all show the homogeneous distribution of Ni and Ag in our $Ag_{0.9}$-$Ni_{0.1}$, $Ag_{0.7}$-$Ni_{0.3}$, and $Ag_{0.3}$-$Ni_{0.7}$ bimetallic NPs and confirm NP alloy formation. In combination with our previous results from $Ag_{0.5}$-$Ni_{0.5}$ NPs,[25] we believe that Ag-Ni alloy NPs can be formed at any ratio of Ni and Ag even though they are immiscible in bulk.

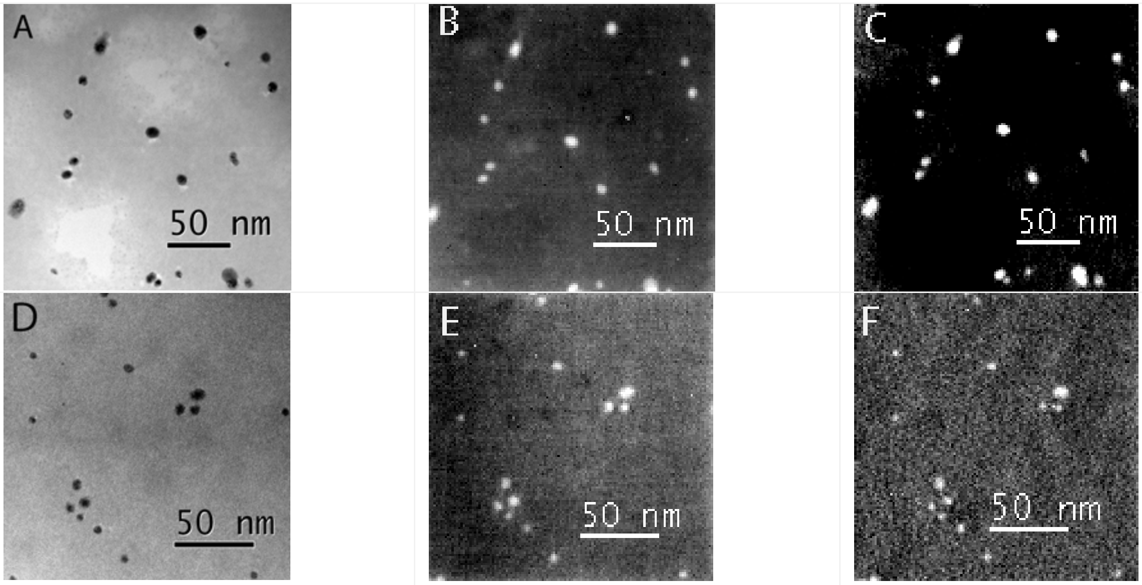

Figure 5. EFTEM maps of $Ag_{0.7}$-$Ni_{0.3}$ NPs (panels A, B, and C) and $Ag_{0.3}$-$Ni_{0.7}$ NPs (panels D, E, and F). For $Ag_{0.7}$-$Ni_{0.3}$ NPs, (A) zero loss image, (B) Ni map, and (C) Ag map. For $Ag_{0.3}$-$Ni_{0.7}$ NPs, (D) zero loss image, (E) Ni map, and (F) Ag map. All scale bars are50 nm.

Heating experiments were carried out to test the stability of these Ag-Ni NPs due to possible dealloying effects as shown by Sastry et al.[34] Similar to the case of $Ag_{0.5}$-$Ni_{0.5}$,[25] results from both HAADF-STEM and EFTEM maps confirmed that the homogeneity of alloy structure of Ag-Ni NPs is retained after mild heating.

Pd-Ni nanoparticles

For Pd-Ni, we were successful in synthesizing and confirming the alloy structure of the $Pd_{0.5}$-$Ni_{0.5}$ NPs. A combination of UV-vis, TEM-HRTEM, HAADF-STEM, and EFTEM mapping methods were used to confirm a homogeneous distribution of Ni and Pd in alloyed $Pd_{0.5}$-$Ni_{0.5}$ NPs.

The UV-vis spectrum is shown for as-synthesized Pd-Ni alloy NPs after 36 min irradiation (curve a) and it indicates no absorption band present (see Fig. 6). Although Mie theoretic calculations indicates Pd has a absorption band around 225 nm,[45] our spectrum of pure Pd NPs does not show any absorption peak around 225 nm. This may be due to interference from the presence of post-irradiated PVA in solution. Furthermore, TEM results of our Pd NPs are similar to those reported by Henglein.[52]

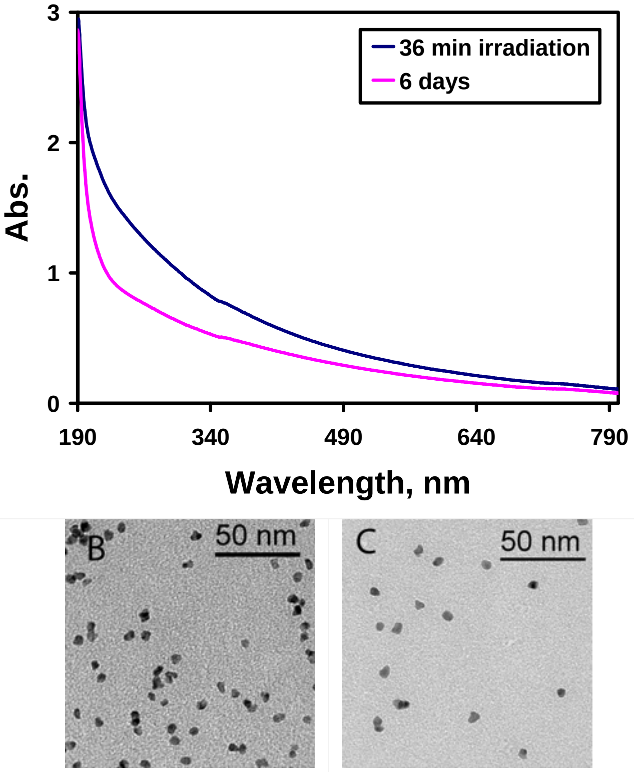

Figure 6. (A) UV-vis spectra of $Pd_{0.5}$-$Ni_{0.5}$ NPs as-synthesized after 36 min irradiation (curve a) and aged after 6 days (curve b) Absorbance is normalized to 1 cm optical path. TEM image of $Pd_{0.5}$-$Ni_{0.5}$ NPs as-synthesized (B), and after 6 days aging (C). Scale bars for both (B) and (C) are 50 nm.

The as-synthesized $Pd_{0.5}$-$Ni_{0.5}$ NPs are not spherical but are in elliptical shape with an aspect ratio of 1.33 (5.1 nm in transverse length and 6.8 nm in longitudinal length). There is a damping in intensity in the UV-vis (see Fig. 6A, curve b) with no change in spectra after 6 days. A ripening process may cause the intensity decrease in UV-vis, but the particle size change is very small with a 0.1 nm increase for both transverse and longitudinal lengths and no change for aspect ratio (see Fig. 6C). In addition, the lattice spacing derived from the HRTEM image shows that 50% Ni and 50% Pd may be present in the alloy NPs. Therefore, both TEM and HRTEM confirm that there is no core-shell structure in our $Pd_{0.5}$-$Ni_{0.5}$ NPs.

HAADF-STEM and EFTEM mapping results for $Pd_{0.5}$-$Ni_{0.5}$ NPs clearly show that Ni and Pd are homogeneously distributed within the whole particle. The HAADF-STEM/ EDX characterization data are presented in Fig. 7. They clearly show that there are no core-shell structures in $Pd_{0.5}$-$Ni_{0.5}$ NPs, with both Ni and Pd being homogeneously distributed throughout each NP. EDX of one Pd-Ni particle shows that both Ni and Pd are present in one single $Pd_{0.5}$-$Ni_{0.5}$ NP. The EFTEM maps of Ni and Pd are presented in Fig. 8. They demonstrate that both Ni and Pd are present in $Pd_{0.5}$-$Ni_{0.5}$ NPs and the spatial distribution of $Pd_{0.5}$-$Ni_{0.5}$ NPs in both images is consistent. The spatial distribution of $Pd_{0.5}$-$Ni_{0.5}$ NPs is also consistent with the corresponding zero loss image in Figure 8A.

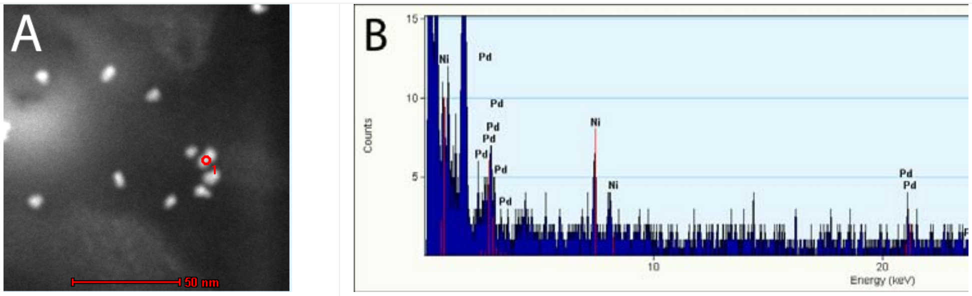

Figure 7. (A) HAADF-STEM image of $Pd_{0.5}$-$Ni_{0.5}$ NPs. Scale bar: 20 nm. (B) Single particle EDX. The particle for EDX analysis is from (A) as indicated by the red circle. The EDX analysis shows the peaks from both Ni and Pd and thus indicates the presence of both elements in one particle.

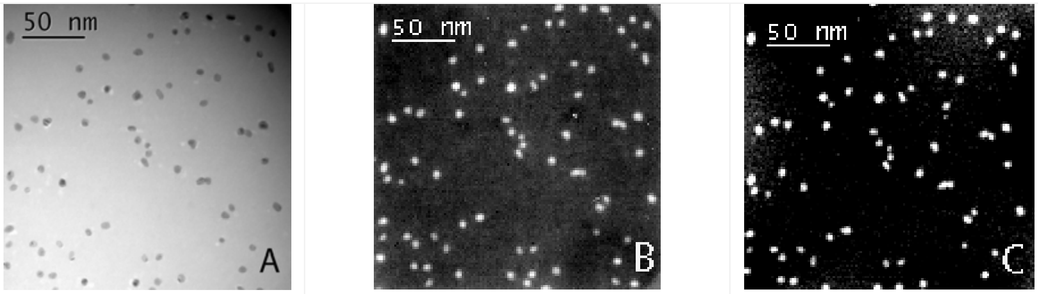

Figure 8. EFTEM maps of $Pd_{0.5}$-$Ni_{0.5}$ NPs. (A) zero loss image, (B) Ni map, and (C) Pd map. All scale bars are50 nm.

Aberration Corrected TEM data.

Aberration corrected TEM data was collected on the both the 50-50 AgNi and PdNi samples. The AC-STEM with the electron probe of less than 0.1nm allows the direct observation atomistic Z-contrast image of the NPs. There is no evidence of core-shell formations in any of the NPs studied; instead a homogenous distribution of the two elements per NP indicate alloying. See Fig 9.

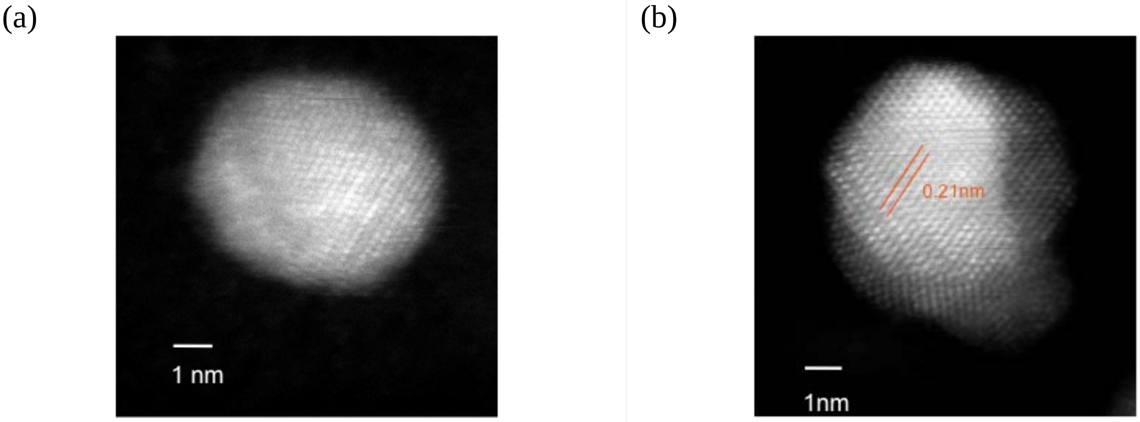

Figure 9. Aberration corrected TEM. HAADF Z-contrast images of (a) AgNi and (b) PdNi

To further confirm the alloying in these NPs, the Z contrast profile and the Pd EELS peak profile data were collected across an individual PdNi NP. Inspection of the data indicates that both sets of data have very similar peak shapes, indicating the uniform distribution of Pd atoms in the particle. See Fig 10.

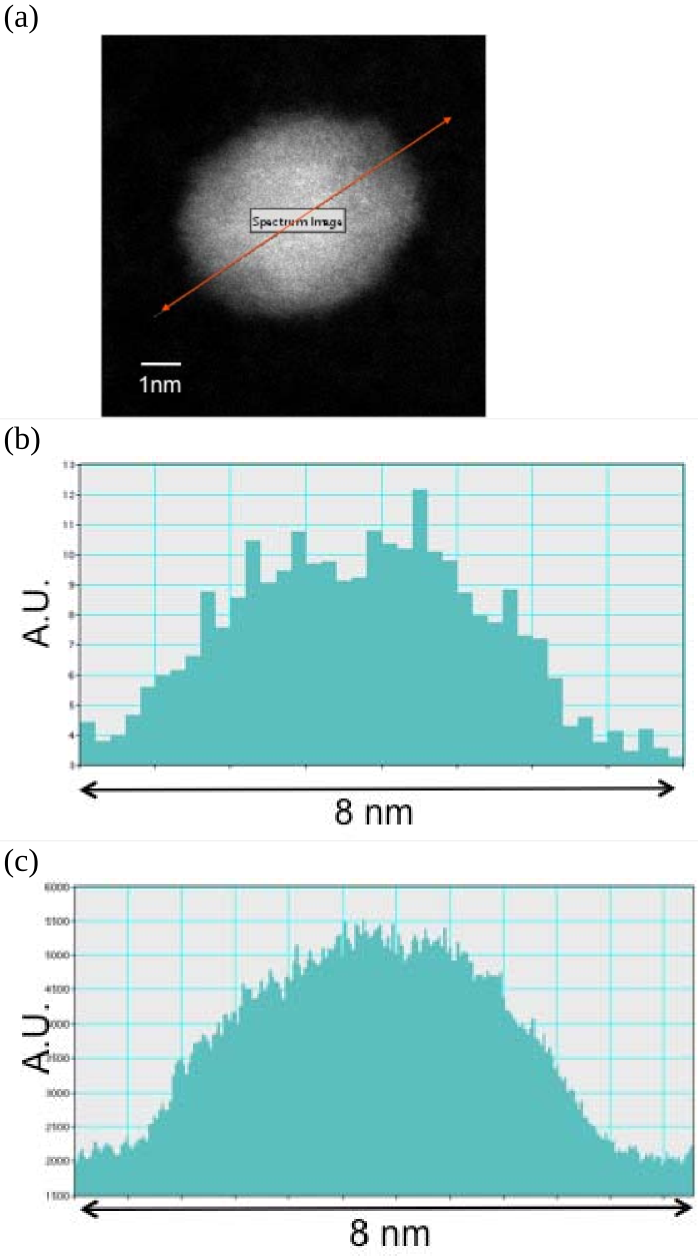

Figure 10. (a) HAADF Z-contrast image of PdNi, (b) Pd EELS peak line profile across the particle, (c) Intensity line-profile in the Z-contrast image (across the particle)

Reaction mechanisms

Our synthesis of any ratio of Ag-Ni alloy NPs is the first successful attempt to obtain stable alloy NPs which are immiscible in bulk. The confirmed alloy structures of Ag_x-Ni_{1-x} NPs, and $Pd_{0.5}$-$Ni_{0.5}$ NPs, have allowed us to propose and elaborate upon the following NP formation mechanism.

NPs formation under radiolysis.

γ-irradiation creates hydrated electrons, H atoms and hydroxyl radicals from water. As indicated in eq1, methanol can scavenge H atoms and hydroxyl radicals. Therefore, hydrated electrons and hydroxymethyl radicals ($\cdot CH_2OH$), the two reducing species formed upon γ-irradiation, may reduce Ag^+ and Ni^{2+} to produce Ag-Ni alloy NPs.

$$\cdot OH\ (\cdot H) + CH_3OH \rightarrow H_2O\ (H_2) + \cdot CH_2OH \qquad (1)$$

The redox potentials of Ag^0 (Ag atom) $E^0(Ag^+/Ag^0)$ and Ag_{bulk} $E^0(Ag^+/Ag_{bulk})$ are at -2.1 V and 0.8 V, respectively if $\Delta G_{sub} = 2.94$ eV for Ag bulk is taken.[24, 53-55] The difference between $E^0(Ag^+/Ag^0)$ and $E^0(Ag^+/Ag_{bulk})$ is the sublimation or atomization energy of silver. While the redox potentials of hydrated electrons and hydroxymethyl radicals ($\cdot CH_2OH$) are -2.7 V[56] and -1.18 V,[57] respectively. Thus, one can expect that it is difficult for hydroxymethyl radicals ($\cdot CH_2OH$, -1.18 V) to reduce Ag^+ to Ag atom ($E^0(Ag^+/Ag^0)$, -2.1 V) in the absence of NPs. Indeed, previous experiments confirmed that it was inefficient (e.g. very low yield of metal atoms) or difficult (e.g. long induction time) for hydroxymethyl radicals ($\cdot CH_2OH$) to reduce Ag^+ in the absence of metallic NPs.[24, 26, 58]

The redox potentials of a Ni atom $E^0(Ni^{2+}/Ni^0)$, Ni^{2+} $E^0(Ni^{2+}/Ni^+)$, and Ni^+ $E^0(Ni^+/Ni^0)$ were reported to be -2.2 V,[59] -2.7 V, and -1.7 V,[60] respectively. However, the first redox value ignored the covalent interactions between water and the Ni atom, while the last redox value contained a simple theoretical estimate of Ni^+ hydration free energy that ignored ligand fields effects.[61] A recent *ab initio* molecular dynamics (AIMD) calculation yielded hydration free energy changes more consistent with Ni^{2+} $E^0(Ni^{2+}/Ni^+)$ -2.2 V[62] after more recent, widely accepted values of Ni ionization potentials were also incorporated.[63] This recent work suggested that previous theoretical estimates of the redox potentials of unstable radiolysis intermediates should be re-examined. Nevertheless, all these $E^0(Ni^{2+}/Ni^+)$ values are consistent with the interpretation that, in the absence of NPs, hydroxymethyl radicals ($\cdot CH_2OH$) cannot transfer electrons to Ni^{2+}.

Therefore, Ni^{2+} and Ag^+ are almost solely reduced by hydrated electrons at the very beginning of the reaction. The redox potential for Pd^{2+}, $E^0(Pd^{2+}/Pd^0)$, is -3.91 V.[64] Similarly, for Pd-Ni NPs, Pd^{2+} and Ni^{2+} can only be reduced by hydrated electrons at the very beginning of the reaction in the absence of NPs, but not reduced by hydroxymethyl radicals ($\cdot CH_2OH$).

Ag-Ni NP nuclei formation.

It is well established that the formation of NPs experiences two stages, nucleation (relatively fast process) and growth (relatively slow process).[65, 66] For the fast nucleation process under irradiation, hydrated electrons generate $(\mathrm{AgNi})_n$ alloy clusters, which, similar to the case of Ag,[67] may have a diameter of less than 1 nm and are the nuclei for particle growth. $(\mathrm{Ag})_n$ and $(\mathrm{Ni})_n$ clusters will be formed if a very low dose rate is applied. As shown above, a high dose rate was used in our experiment (300 rad/s), and our EFTEM mapping results show no small Ag or Ni NPs formed. $(\mathrm{AgNi})_n$ formation from high dose rates is due to kinetic competition, i.e., an intermetallic electron transfer quench mechanism as shown below. In the case of Pd-Ni NPs, similarly, initial $(\mathrm{PdNi})_n$ alloy clusters can be generated by hydrated electrons.

Ag-Ni NP growth stage.

After $(\mathrm{AgNi})_n$ nuclei are formed, a nanoparticle growth stage begins. For the growth stage, radicals can transfer electrons to nuclei or small metallic particles and form the so called electron pool on nuclei or small particles.[24, 26, 68] In our case, the tiny $(\mathrm{AgNi})_n$ nuclei clusters can get electrons from hydroxymethyl radicals ($\cdot\mathrm{CH_2OH}$) and electron pools (eq 2) are generated, similar to the case of Pd NP formation.[52] $\mathrm{Ag^+}$, $\mathrm{Ni^{2+}}$, and $\mathrm{Ni^+}$ ($\mathrm{Ni^{2+}}$ may undergo $e_{aq}^-/\ \cdot\mathrm{CH_2OH} + \mathrm{Ni^{2+}} \rightarrow \mathrm{Ni^+}$, $2\mathrm{Ni^+} \rightarrow \mathrm{Ni^0} + \mathrm{Ni^{2+}}$) in solution can accept electrons from the charged $(\mathrm{AgNi})_n$ clusters and get reduced at the surface of these clusters. However, there are also reports that $\mathrm{Ni^+}$ disproportionation reactions into $\mathrm{Ni^0}$ and $\mathrm{Ni^{2+}}$ do not occur spontaneously.[69] Such growth process of $(\mathrm{AgNi})_n$ finally leads to the formation of Ag-Ni NPs. Hydrogen formation by stored electrons in $(\mathrm{AgNi})_n$ clusters and radical-radical reactions can be the competing reactions of the above growth process.[26, 70] However, these reactions do not have a significant effect on particle formation as confirmed by experiments and calculations which were based on reaction conditions similar to ours.[26] Similarly, in the case of Pd-Ni, hydroxymethyl radicals ($\cdot\mathrm{CH_2OH}$) can donate electrons to $(\mathrm{PdNi})_n$ nuclei clusters and lead to the growth process of $(\mathrm{PdNi})_n$ clusters as shown in eq 3.

$$x\cdot\mathrm{CH_2OH} + (\mathrm{AgNi})_n \rightarrow (\mathrm{AgNi})_n^{x-} + x\mathrm{CH_2O} + x\mathrm{H^+} \quad (2)$$

$$x\cdot\mathrm{CH_2OH} + (\mathrm{PdNi})_n \rightarrow (\mathrm{PdNi})_n^{x-} + x\mathrm{CH_2O} + x\mathrm{H^+} \quad (3)$$

A model for Au-Ag alloy NP formation under high dose rates was developed by Belloni et al.[71] In short, the model describes how high dose rates (35 kGy/h, i.e. 972 rad/s) practically block intermetallic electron transfer between noble core metals and the less noble metal ions in solution. As a result, there is a sudden reduction of all metal ions in solution that makes the charge transfer between more noble ions (e. g., $\mathrm{Au^+}$) and less noble atoms (e. g., Ag) impossible (shown in eq 4 and 5). This results in homogenous alloy NP formation.[71, 72]

$$\mathrm{N} + \mathrm{M^+} \rightarrow (\mathrm{NM})^+ \rightarrow \mathrm{N^+} + \mathrm{M} \qquad (4)$$

$$(\mathrm{M}_m\mathrm{N}_n)^{x+} + \mathrm{M^+} \rightarrow (\mathrm{M}_{m+1}\mathrm{N}_n)^{(x+1)+} \rightarrow (\mathrm{M}_{m+1}\mathrm{N}_{n-1})^{x+} + \mathrm{N^+} \qquad (5)$$

where N is the less noble metal (e.g., Ag) and M is the more noble metal (e.g., Au).

Similar to earlier reports on NP alloy formation by radiolysis,[25,71] high dose rates reduce the Ag and Ni ions within a very short time, shorter than any other electrochemical or thermodynamic process. Therefore, it can mostly suppress the possible intermetallic electron transfer between Ag and Ni ions or atoms. High dose rates result in the formation of an alloy structure which has the same metal ratio as their ionic precursors because both metal atoms are quenched suddenly into the lattice. The intermetallic electron transfer quench mechanism also occurs in the two stages, nucleation and growth, and is complimentary for the whole particle formation process from the kinetic aspect. Such a mechanism explains that kinetically favored alloy structure can be formed with very fast reducing rate.

Pd-Ni NP formation.

Similar to Ag-Ni alloy NP formation, a high dose rate reduces Pd and Ni ions simultaneously. Possible intermetallic electron transfer is quenched between Pd and Ni ions or atoms, resulting in the formation of the Pd-Ni kinetically favored alloy NP structure.

DFT modeling of alloy versus core-shell, Ag-Ni NPs.

To confirm the fact that the NP creation was kinetically and not thermodynamically determined, we used DFT to consider the energies of representative NPs. The initial and final configurations of a Ni core-Ag shell particle are seen in Fig. 11. As Ni is more reactive and has a much higher surface energy than Ag, this configuration should be favored, as was indeed found to be the case. The final configuration was found to retain a C_{3v}-like geometry (which was not imposed in the calculation) and exhibited a 0.55 μ_B magnetization per Ni atom. Two randomly generated Ag-Ni alloy NPs are depicted in Figs. 11C and D. They exhibited energies 49.5 and 43.7 eV higher than the Ni-core NP, respectively. Their magnetizations were 0.53 and 0.56 μ_B per Ni atom.

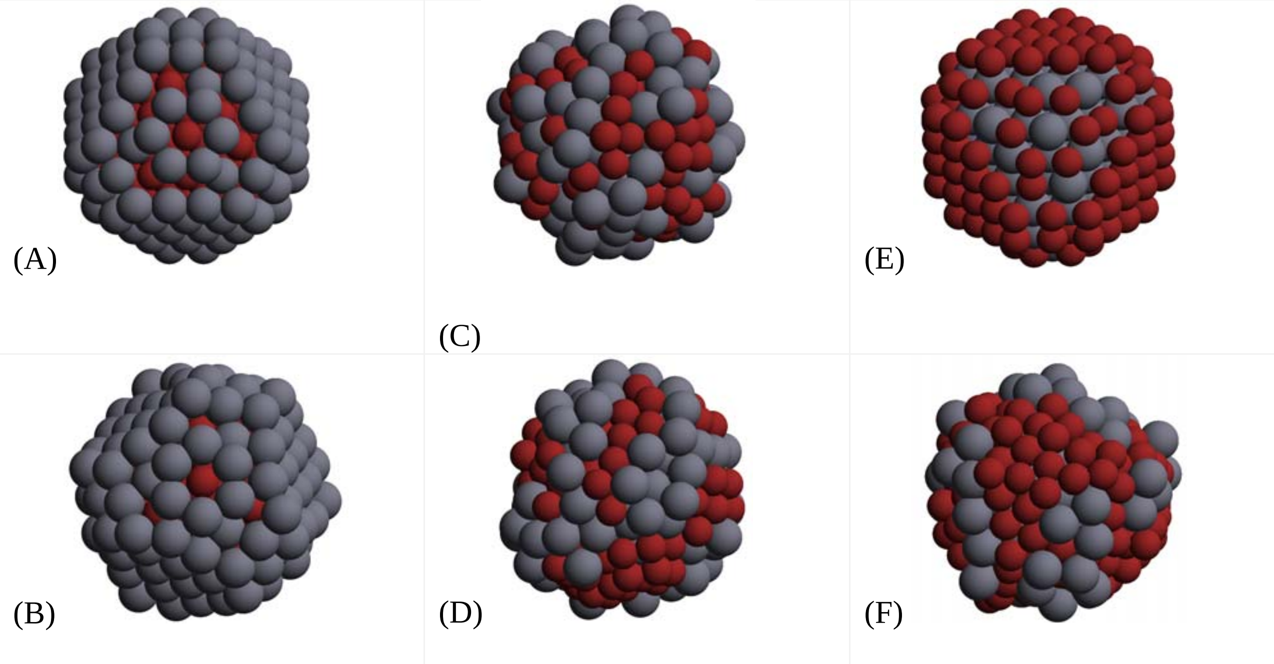

Figure 11. NP models containing 120 Ag and Ni atoms each. (A) and (B): initial and final Ni core-Ag shell configurations. (C) and (D): final configurations of two random alloy NP. (E) and (F): initial and final Ag core-Ni shell configurations.

Finally, the initial and final configurations of the Ag core-Ni shell NP are depicted in Figs. 11 (E) and (F). Since this core-shell NP exposed a maximum number of Ni atoms at the surface, it was initially unstable and experienced large structural changes during structural relaxation from its initial FCC lattice structure. The final local minimum configuration exhibited some Ni_4 tetrahedral motifs, not just a single layer of Ni at the surface, to alleviate surface energy costs. Furthermore, some Ag atoms were ejected to the surface. Despite all these structural changes, the energy of this NP remains the highest among all examined, 57.2 eV above the Ni core NP. The magnetization was also the largest, at 0.59 μ_B per Ni atom, reflecting the high Ni surface fraction.

Even though our conjugate gradient procedure could only search for local minima in the potential energy surface, the Ni core structure was significantly more favorable than random alloy structures which exposed Ni atoms at their surfaces. Despite their stability, Ni core structures were not observed in our γ-radiolysis synthesis experiments. Thus, the NP formation must be kinetically controlled.

DFT modeling of alloy versus core-shell, Pd-Ni NPs.

The Pd-Ni total energy calculations show a clear preference for Ni core-Pd shell structure with -17.8 eV energy gain to the reference (Fig. 12A), while Pd core-Ni shell is 22.8 eV higher than the pure reference (Fig. 12B), i.e., 40.6 eV higher than Ni core-Pd shell. The energy range for the 4 random clusters is from -1.2 eV to 2.2 eV. The relative energy for the two layered alloys is -1.5 eV (Fig. 12C) and 2.9 eV. This DFT simulation further confirms that the formation our $Pd_{0.5}$-$Ni_{0.5}$ alloy NPs is kinetically controlled. Additional reports have shown that Pd-Ni alloy NPs,[10] Ni core-Pd shell,[28] and Pd core-Ni shell[27] NPs were synthesized by either a one step co-reduction (to form alloy) or a stepwise (to form core-shell) approach, although Pd core-Ni shell NPs are thermodynamically unfavorable.

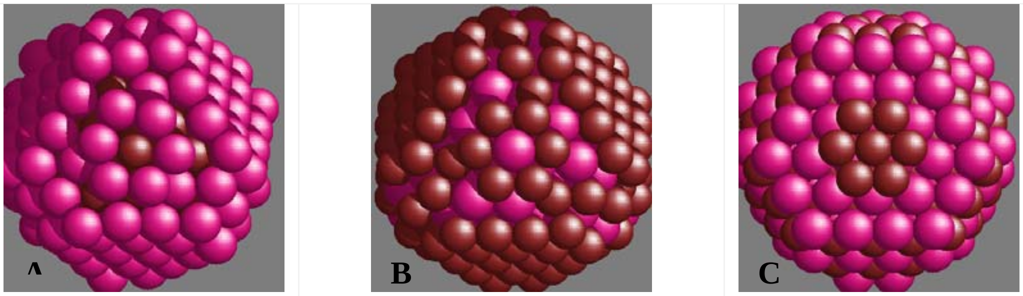

Figure 12. NP models containing 120 Pd and Ni atoms each. (A) Ni core-Pd shell configuration. (B) Pd core-Ni shell configuration. (C) layered Pd-Ni structure.

Conclusion

Room temperature radiolysis, density functional theory, and various nanoscale characterization methods were used to synthesize and fully describe Ni-based alloy NPs which were synthesized at room temperature. These complementary methods provide a strong basis to understand and describe NPs whose reaction formation is via kinetic processes, rather than thermodynamic processes. Furthermore, radiolysis has proven to be a method by which we can access novel metastable phase regimes not previously found by traditional alloying techniques. The experimentation, characterization, and DFT modeling combined to fully describes the formation of silver and palladium Ni-based alloy NPs.

We have demonstrated that different stoichiometries of Ag-Ni alloy NPs and $Pd_{0.5}$-$Ni_{0.5}$ alloy NPs can be synthesized at room temperature by this high dose rate radiolytic method. The Ag_x-Ni_{1-x} and $Pd_{0.5}$-$Ni_{0.5}$ NPs were fully characterized by UV-vis, TEM/HRTEM, HAADF-STEM, and EFTEM mapping. The analysis results clearly show that homogenous alloy NPs were made, as opposed to core-shell NPs. Our reaction mechanism indicates that the metal precursor ions were reduced simultaneously by high dose rate of γ-irradiation and that alloy NPs were formed in varying Ag-Ni ratios and also in the 50%Pd-50%Ni ratio. Single particle EDX shows that both Ag/Ni and Pd/Ni, respectively, are present within each particle. The consistency from both shape and spatial distribution of NPs in EFTEM maps indicate that both Ag (or Pd) and Ni are present, and both components are homogeneously distributed within the whole particle. In addition, our results from EFTEM map show that Ni and Ag are present in a wide variety of ratios for Ag-Ni NPs ($Ag_{0.9}$-$Ni_{0.1}$, $Ag_{0.7}$-$Ni_{0.3}$, $Ag_{0.5}$-$Ni_{0.5}$, and $Ag_{0.3}$-$Ni_{0.7}$) and the homogeneity is retained.
We have used Ag-Ni as an example to illustrate the mechanism of the alloy formation. Silver and nickel ions are reduced by hydrated electron to form nuclei first, and then nuclei growth is facilitated by electron pools. The final structures of bimetallic NPs are determined by the dose rates used in the reaction. The high dose rate employed in this study can reduce Ag and Ni ions within a very short time and thus can overcome intermetallic electron transfer induced, or thermodynamic favorable, core-shell formation.

Radiolysis provides us an important (and possibly a universal) method of synthesizing uniform alloy NPs, in metastable phase regimes not accessible by traditional methods. Alloy NPs of other immiscible metal pairs, which do not react with water, may also be prepared by radiolytic method or other methods which can reduce metallic precursors very quickly. Our ongoing research is focused on both the reducibility and subsequent NP formation of other transition metals into a Ni-based system, and the sintering of all of our synthesized NPs into bulk phases for future mechanical testing. We also plan to continue using AIMD theoretical techniques to investigate redox potentials for small homonuclear (e.g., mono- and di-atomic) and bimetallic clusters.

II. SuperAlloy Nanoparticles

Introduction

Superalloys are phases that are high temperature, corrosion resistant inorganic materials with both defense and civilian applications. The addition of refractory elements to the traditional Ni based systems "hardens" the material to even higher temperatures, while retaining their superb mechanical strength. Traditionally, alloys are synthesized by a variety of methods including melt casting and sintering. Sintering is the preferred method (as compared to melting) as it will not destroy the refractories. It is anticipated that the radiolysis process will result in more defect-free superalloy metals, allowing for more energy efficient (lower process temperatures) and wider ranges of alloy compositions to be synthesized.

After succeeding in our synthesis on AgNi and PdNi alloy nanoparticles, we began the research on superalloy nanoparticle compositions including CoNi and WNi. The superalloy NPs synthesis attempts are 50/50 concentration ratios using high dose rates from gamma irradiation. The results presented include the completed NP syntheses and characterizations.

Experimental

In the synthesis, different stoichiometries of W-Ni NPs were prepared using the following radiolytic methodology: a 50 mL aqueous solution containing 0.6 to 2 × 10^{-4} M Na_2WO_4, 1.4 to 0 × 10^{-4} M $NiSO_4$, 3 × 10^{-4} M sodium citrate, 0.5 M methanol, and 1.5 × 10^{-2} M poly-vinyl alcohol (PVA, M_w, 88,000) were deaerated by bubbling Ar for 12 mins, and then irradiated in a ^{60}Co-γ source (Sandia National Laboratories Gamma Irradiation Facility (GIF)) at a dose rate of 435 rad/s for 37 mins. The total concentration of different stoichiometries of W and Ni ions was kept at 2 × 10^{-4} M (see Table 4). Similarly, for the $Co_{0.5}$-$Ni_{0.5}$ (50% Co and 50% Ni) alloy NPs preparation, a 50 mL aqueous solution containing 1 × 10^{-4} M $CoCl_2$, 1 × 10^{-4} M $NiSO_4$, 3 × 10^{-4} M sodium citrate, 0.5 M methanol, and 1.5 × 10^{-2} M poly-vinyl alcohol (PVA, M_w, 88,000) was irradiated at a dose rate of 435 rad/s for 36 min.

Table 4. Different stoichiometry of W, Co and Ni ions used to prepare W-Ni and Co-Ni alloy NPs.

	W	$W_{0.5}$-$Ni_{0.5}$	$W_{0.3}$-$Ni_{0.7}$		Co	$Co_{0.5}$-$Ni_{0.5}$
[WO_4^{2-}] × 10^{-4} M	2	1	0.6	[Co^{2+}], × 10^{-4} M	2	1
[Ni^{2+}], × 10^{-4} M	0	1	1.4	[Ni^{2+}], × 10^{-4} M	0	1
[WO_4^{2-}] + [Ni^{2+}], × 10^{-4} M	2	2	2	[Co^{2+}] + [Ni^{2+}], × 10^{-4} M	2	2
[WO_4^{2-}]:[Ni^{2+}]	pure W NPs	1:1	3:7	[Co^{2+}]:[Ni^{2+}]	pure Co NPs	1:1

The reaction was carried out in a 100 mL vessel which was equipped with a sidearm containing a 0.5 cm optical path, and was sealed with two septa. This allowed for the collection of UV-vis spectra without exposing the solution to air. Full reduction of the metal ions was determined when there was no change in UV-vis spectra upon additional irradiation. Specimens for TEM were prepared by dropping the solution on a titanium-carbon grid and subsequent drying under N_2 gas in a glovebox.

Characterization.

UV-vis absorption spectra were taken on a Varian Cary 300 Scan UV-Visible Spectrophotometer. Mean particle diameters, particle size distribution, and morphology were determined by using a JEOL 1200EX (120 kV) bright-field transmission electron microscopy (TEM) with Gatan digital imaging. High-resolution TEM and scanning TEM (STEM) images were acquired using an FEI Tecnai G(2) F30 S-Twin (300 kV) TEM at the Center for Integrated Nanotechnologies at Sandia National Laboratories (SNL CINT). This instrument is equipped with Z-contrast capability (to image different elements) with a resolution of 0.14 nm in high-angle annular dark-field (HAADF) mode. The unit is also equipped with energy-dispersive X-ray (EDX) analysis for detection of characteristic X-rays for elemental analysis, and with an electron energy-loss spectrometer (EELS) for characterizing composition and energy-filtered imaging.

Results and Discussion

The two series of NPs, W-Ni and Co-Ni, were analyzed and characterized by a variety of methods, including UV-vis, TEM/HRTEM, HAADF-STEM and EFTEM mapping.

W-Ni nanoparticles. W-Ni alloy NPs with varying stoichiometries (see Table 4) were prepared under similar reaction conditions (e. g. same total metal concentrations, same concentrations of stabilizers, and same irradiation time) and their UV-vis spectra are shown in Figure 13. Figure 13B and C show the UV spectra of 37 min irradiation and 7 days of aging. They look very similar. For the peak around 200 nm, there is a damping effect from pure W to $W_{0.3}$-$Ni_{0.7}$ NPs. Please note that these peaks are also very similar to those before irradiation (Figure 13A). Therefore, the peak around 200 nm may be from some component in the solution.

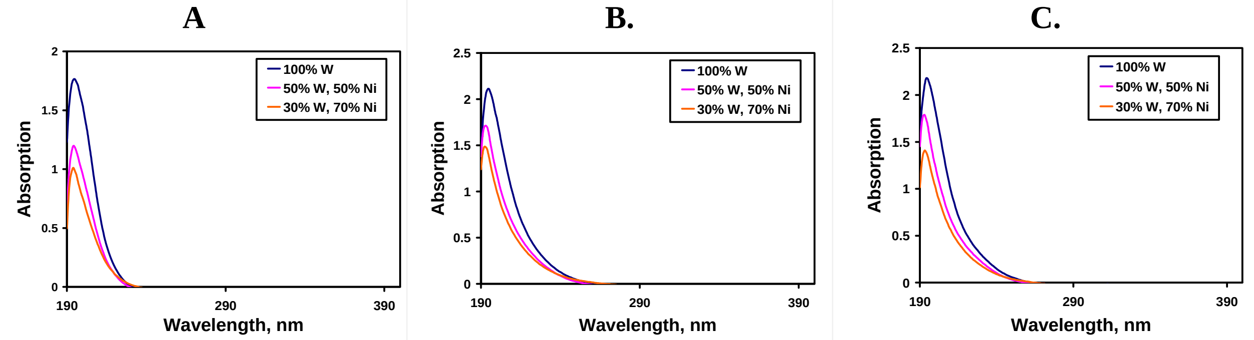

Figure 13. UV-vis spectra of W-Ni NPs. (A) before irradiation. (B) after 37 min irradiation (full reduction). (C) after 7 days of aging. Absorbance is normalized to 1 cm optical path.

The TEM results of pure W NPs are seen in Figure 14. Figure 14A and B show the HRTEM and its corresponding EDX image. The definitive presence of Oxygen in the EDX is unique to this composition study. Figure 14C shows the 490K TEM image. The particle size is about 3-4 nm. Figure 14D shows the diffraction pattern of the NPs. The above results suggest that tungsten oxide particles may be formed instead of W metal nanoparticles. The formation of oxide NPs may be from a reaction between W and water or from the TEM grids preparation, i.e. oxygen in glovebox. An attempt at EFTEM mapping to show the existence of oxygen was not successful, probably because the NPs are too densely arranged on the TEM grid.

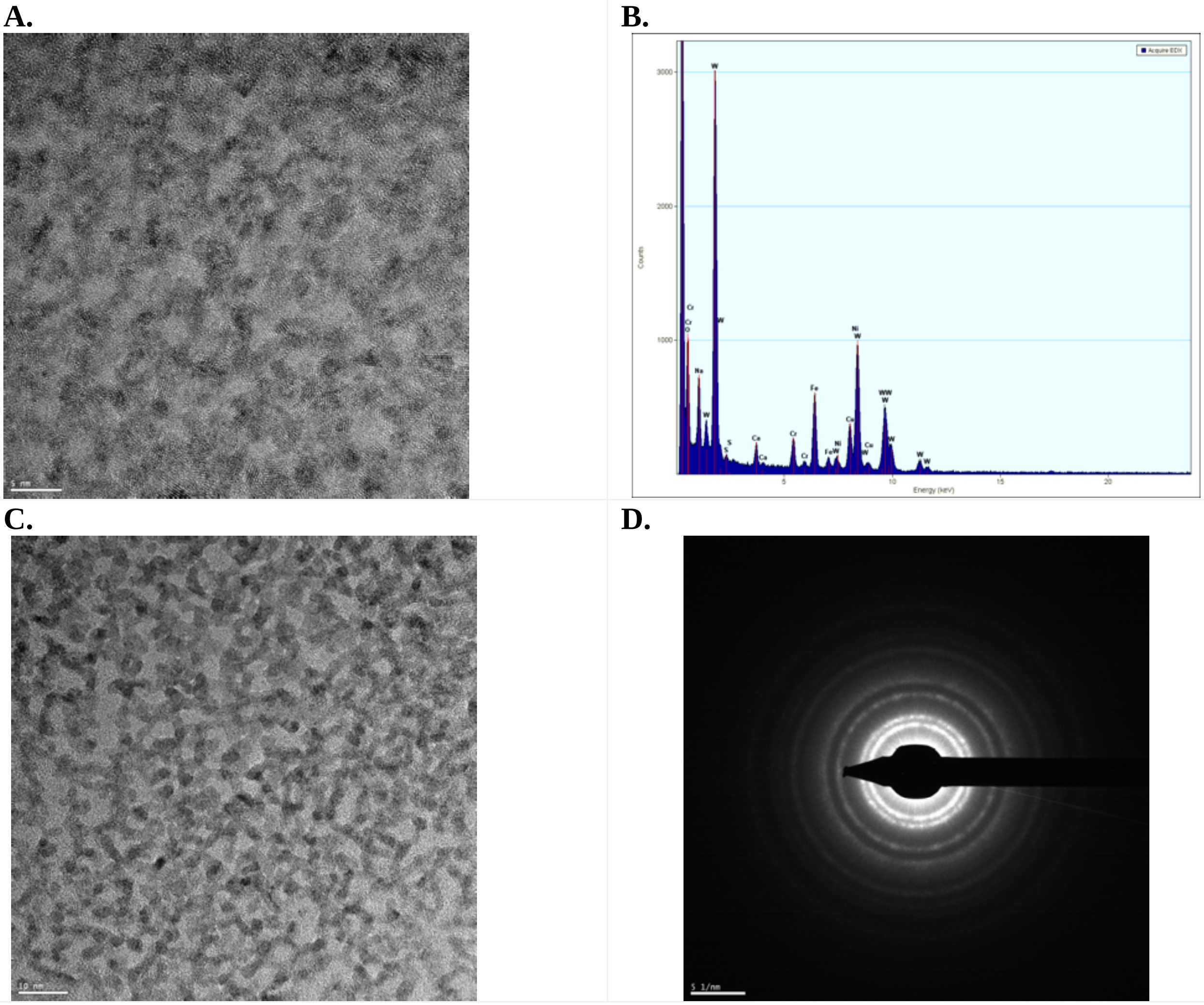

Figure 14. TEM results of pure W NPs. (A) HRTEM (B) EDX analysis from the area in A. (C) TEM image at 490 K. (D) Diffraction pattern of W NPs.

The HRTEM results of $W_{0.5}$-$Ni_{0.5}$ NPs are seen in Figure 15. Figure 15A to D show that the TEM grid was damaged under the beam. These TEM specimens were prepared on Au grids. We believe Ti grids might help with the experimental stability issues. However, we were still able to obtain particle size information about the sample. At first, particle size measured 2nm (Figure 15A). But with time, the particles grew to 5nm (Figure 15D). We were not able to obtain lattice spacing information on these samples. However, in conjunction with the results of pure W NPs, we can assume that W-Ni-O NPs were formed for $W_{0.5}$-$Ni_{0.5}$ NPs.

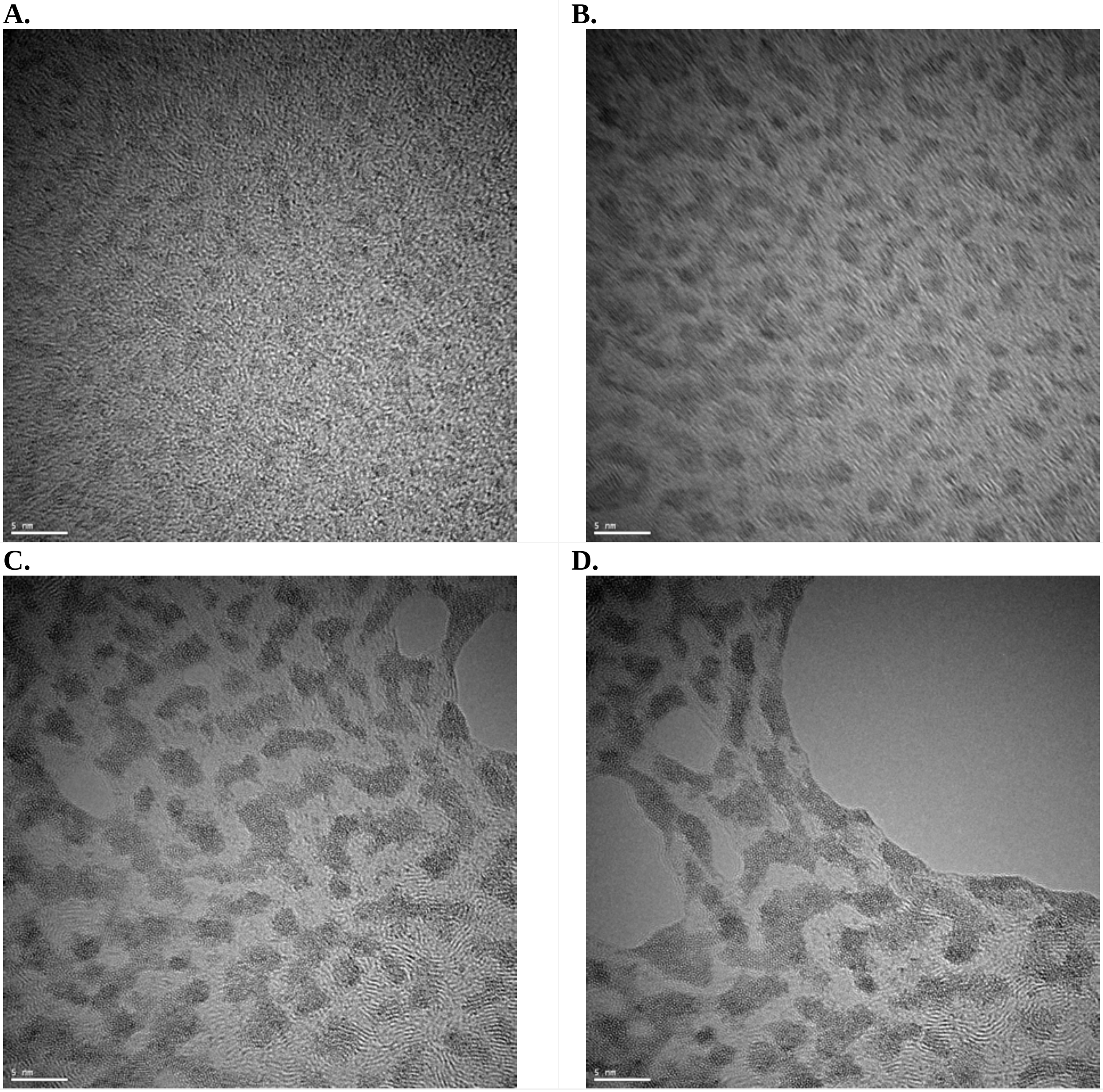

Figure 15. HRTEM results of $W_{0.5}$-$Ni_{0.5}$ NPs. A to D show the process that TEM grid was damaged under the beam

We also studied Co and $Co_{0.5}$-$Ni_{0.5}$ NPs. The Co NP analysis is inconclusive. The Co solution was irradiated for 36 min at 435 rad/s. The UV-vis spectra shape (Fig. 16) is not smooth or consistent with similar experiments. We are concerned with the reliability of this UV-vis data as shortly after data collection this instrument stopped due to mechanical issues. Furthermore, for pure Co NPs, the HRTEM results (Figure 17A) show that the NPs are coagulated on TEM grids. Figure 17B show the TEM image at 195K.

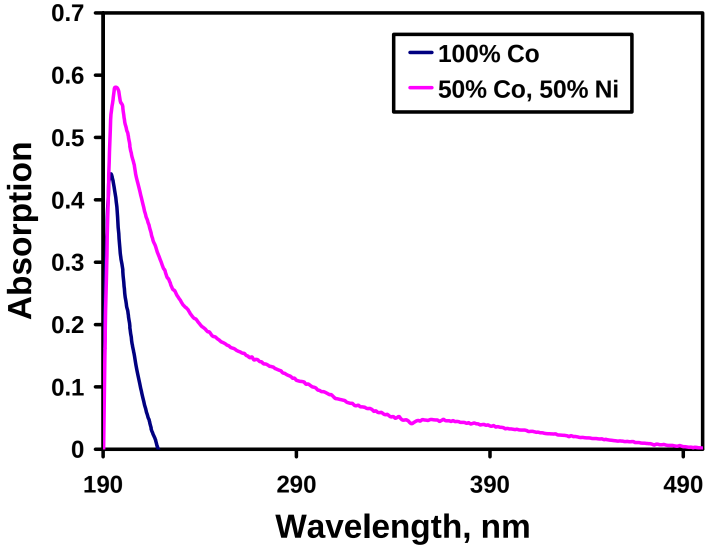

Figure 16. UV-vis spectra of Co-Ni NPs after 37 min irradiation (full reduction). Absorbance is normalized to 1 cm optical path.

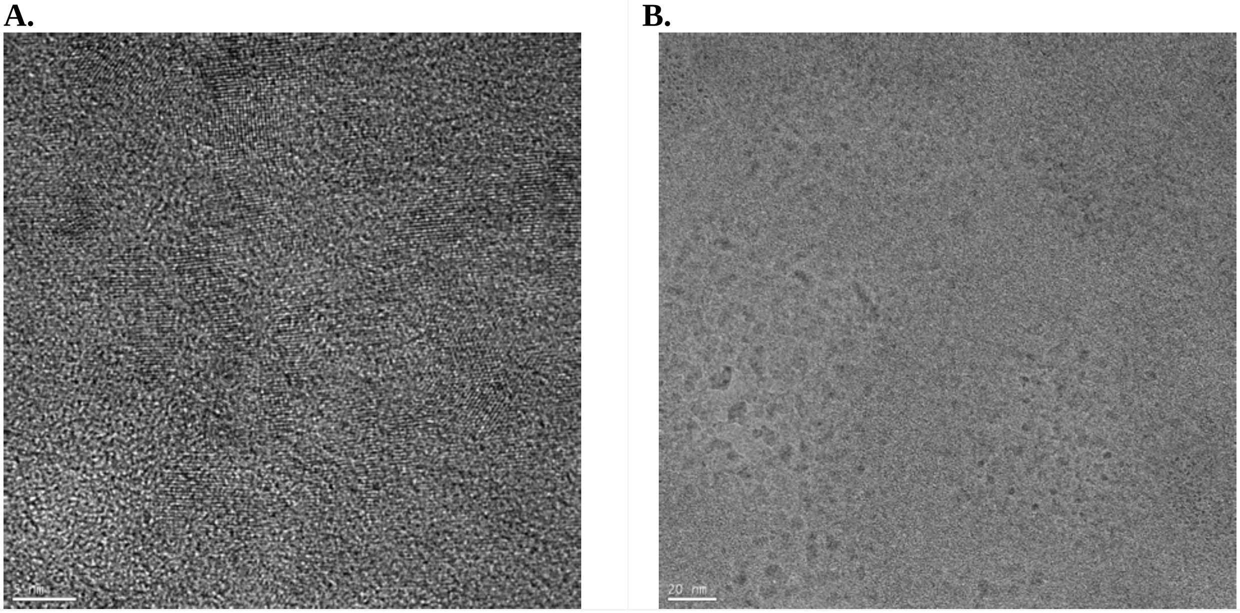

Figure 17. (A) HRTEM of Co NPs. (B) TEM image of Co at 195K.

Analysis of the $Co_{0.5}$-$Ni_{0.5}$ NPs by TEM resulted in some more definitive results. Though there were some instances of beam damage to the grids, we were able to identify a bi-modal particle size distribution by TEM at 145K (Figure 18B). EDX analysis (Figure 18C) of the area in Figure 18B shows 30% Co and 70% Ni.

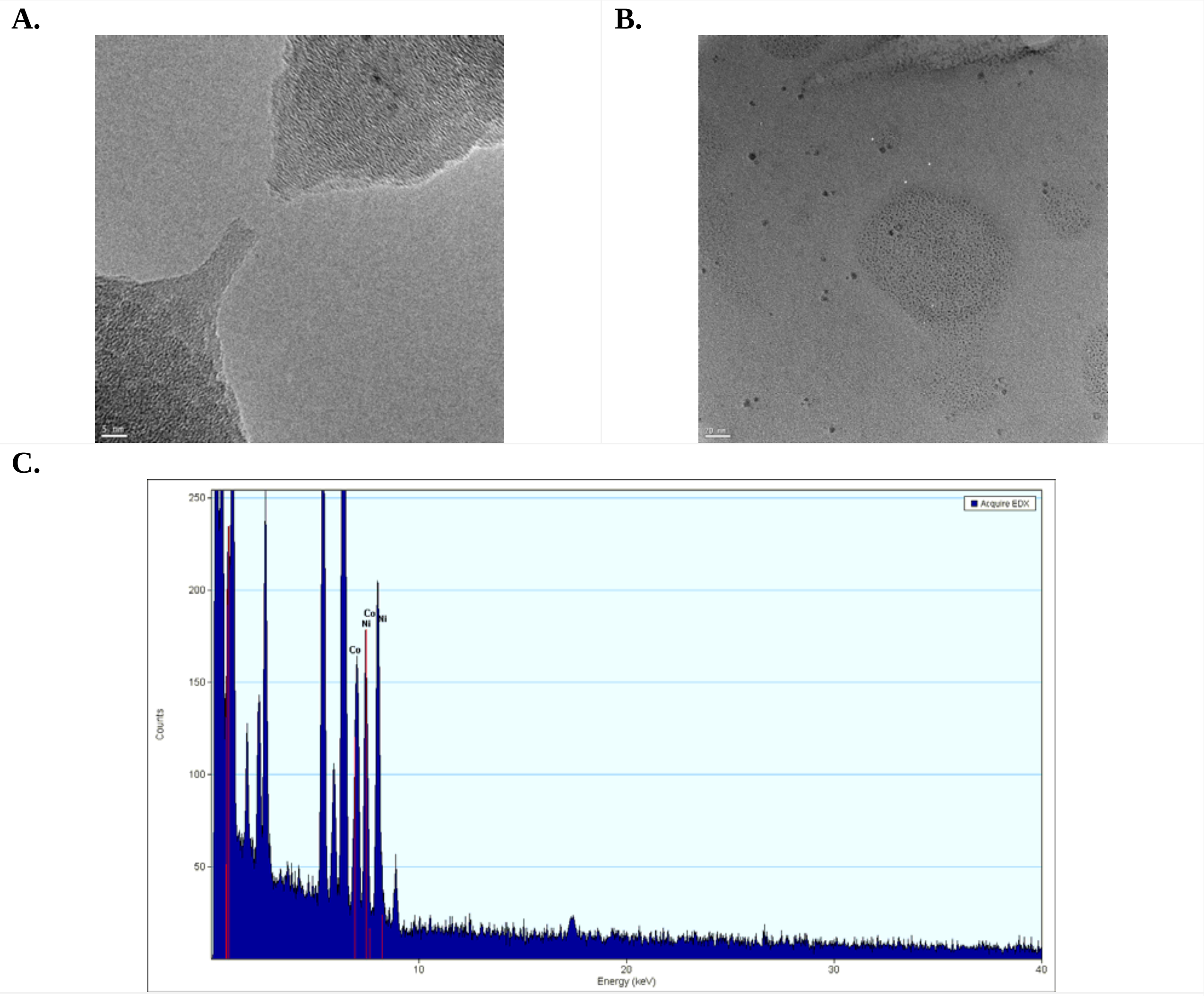

Figure 18. (A) HRTEM image shows some damaged area on grid. (B) TEM image at 145 K shows the bi-model particle size distribution. (C) EDX analysis of corresponding area in B shows 30% Co and 70% Ni.

The HRTEM image of $Co_{0.5}$-$Ni_{0.5}$ NPs and corresponding EDX analysis are seen in Fig. 19A and B, respectively. The EDX analysis indicates 36% Co and 64% Ni. Figure 19C and D show the single particle EDX analysis and the result is 28% Co and 72% Ni, although with some noise. EELS results indicate both Co (left, around 780 eV) and Ni (right, around 850 eV) peaks are present (see Fig. 19E).

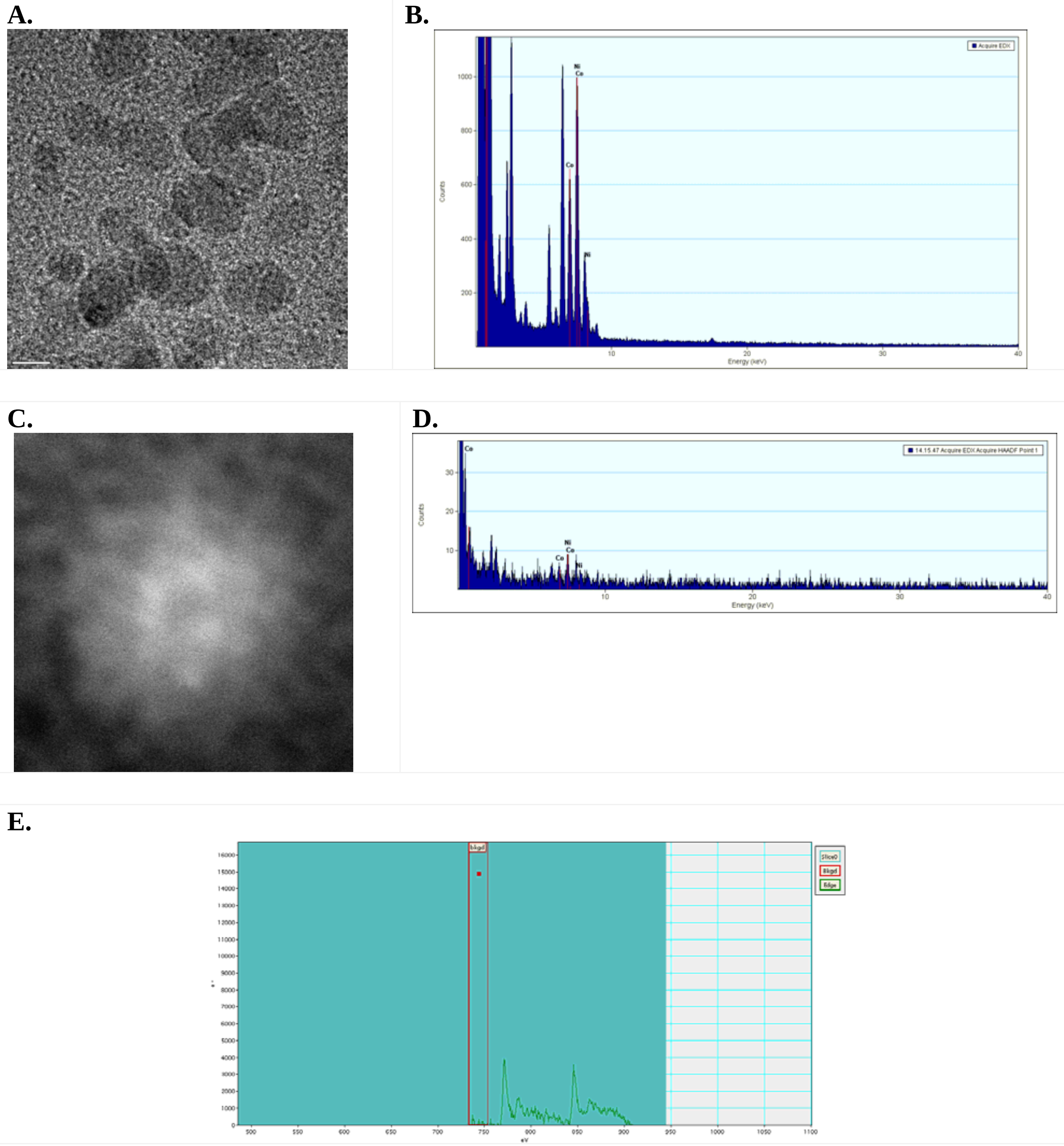

Figure 19. (A) HRTEM image of $Co_{0.5}$-$Ni_{0.5}$ NPs. (B) Corresponding EDX analysis in A shows 36% Co and 64% Ni. (C) STEM image of $Co_{0.5}$-$Ni_{0.5}$ NPs at 3.1 M. (D) EDX analysis of single particle in C shows 28% Co and 72% Ni. (E) EELS result shows both Co (left) and Ni (right) peaks.

Conclusion

As with the earlier alloy NPs, no evidence of core-shell metal NP formation occurs leading us to postulate alloy formation. Microscopy results seem to indicate alloying occurred with the CoNi alloys. The NPs are exceptionally small, on the order of ≈2nm; we are unable at this time to obtain lattice spacings from the HRTEM. Furthermore, single particle EDS and EELS data do indicate that individual NPs contain both Ni and Co, with ≈ 28% Co, 72% Ni (as supported by broad range EDS).

The success with the CoNi NP superalloy does not seem to extend to the WNi NPs. Experiments in which Na_2WO_4 was used as the reactant for single metal NP formation, resulted in the incomplete reduction to the W^{2+} ion in solution; the predominance of WO^+ ion in solution directed coalescence to the formation of WO NPs. This incomplete reduction apparently also occurs in the superalloy attempts of W-Ni NPs. Instead of alloy formation, it appears that individual W-O-Ni NP complexes are isolated as products in solution. It is important to note that these NPs have not yet been fully characterized. Further characterization by aberration corrected TEM at LBNL may elucidate the structure further.

III. Sintering of Nanoparticles

The sintering of NPs to high densities (>85%) cannot be achieved using traditional sintering methods. However, the melting points of nanoparticles are greatly reduced as compared to bulk materials sintering occurs at about two-thirds of suppressed melting temperatures, since the surfaces of nanoparticles have melting points that are lower than those of their cores.[73]
In an effort to study at what temperature our Ni-based NPs sinter, we have begun NP sintering experiments at SNL/CA. This work was performed on a heated-stage TEM to reveal sintering temperatures and mechanisms. Equipment used included a JEOL 2010F field emission electron microscope in a bright field imaging mode at 200kV and a Gatan model 652 heating stage (range 25 – 800°C).

To date, we have completed the high temperature sintering of the 50/50 AgNi NPs. They were deposited from solution onto a Ti grid, and heated from RT to 800°C. Small scale ripening occurs slowly (≈25min) from RT to 450°C. However, from 450 – 800°C, rapid large scale sintering occurs on the NPs. The NPs grow to a size of ≈ 100-150 nm in size. A film of the growth, possibly via Ostwald ripening, is archived at SNL/NM & CA. Fig. 20 shows NP sizes at both 450 and 800°C. Electron diffraction to determine alloy phase integrity versus elemental segregation is on-going.

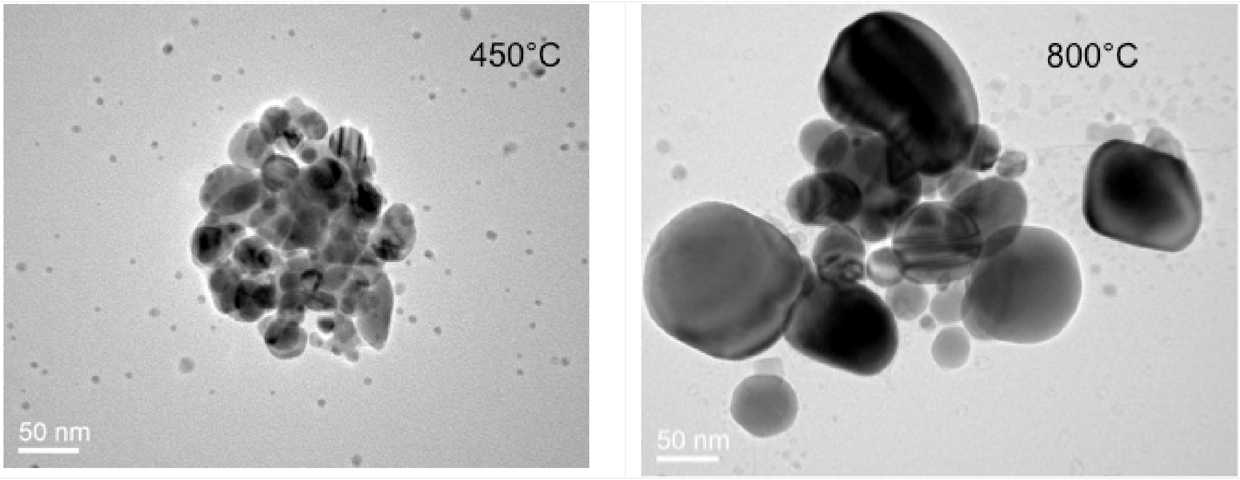

Figure 20. Sintering of AgNi NPs on heated TEM stage.

Ongoing research in this area is focused on determining lattice spacings and elemental composition of the NPs, both before and after sintering. This will provide information as to whether the sintering allowed the alloy structure to be retained, or if elemental segregation occurred.

IV. References

1. C. T. Sims, N. S. Stoloff and W. C. Hagel, *Superalloys*, John Wiley & Sons, 1987.
2. G. Song, N. Ma and H. N. Li, *Eng. Struct.*, 2006, **28**, 1266-1274.
3. T. Yoneyama and S. Miyazaki, *Shape Memory Alloys for Biomedical Applications*, Woodhead Publishing Ltd., Cambridge, UK, 2008.
4. N. W. Ockwig and T. M. Nenoff, *Chem. Rev.*, 2007, **107**, 4078-4110.
5. J. R. Groza, *Nanostruct. Mater.*, 1999, **12**, 987-992.
6. A. M. Molenbroek, J. K. Norskov and B. S. Clausen, *J. Phys. Chem. B*, 2001, **105**, 5450-5458.
7. F. Besenbacher, I. Chorkendorff, B. S. Clausen, B. Hammer, A. M. Molenbroek, J. K. Nørskov and I. Stensgaard, *Science*, 1998, **279**, 1913-1915.
8. M. Veith, N. Lecerf, S. Mathur, H. Shen and S. Hufner, *Chem. Mater.*, 1999, **11**, 3103-3112.
9. Y. Yamauchi, S. S. Nair, T. Momma, T. Ohsuna, T. Osaka and K. Kuroda, *J. Mater. Chem.*, 2006, **16**, 2229-2234.
10. P. Lu, T. Teranishi, K. Asakura, M. Miyake and N. Toshima, *J. Phys. Chem. B*, 1999, **103**, 9673-9682.
11. S. H. Sun, C. B. Murray, D. Weller, L. Folks and A. Moser, *Science*, 2000, **287**, 1989-1992.
12. S. H. Sun, S. Anders, T. Thomson, J. E. E. Baglin, M. F. Toney, H. F. Hamann, C. B. Murray and B. D. Terris, *J. Phys. Chem. B*, 2003, **107**, 5419-5425.
13. E. V. Shevchenko, D. V. Talapin, H. Schnablegger, A. Kornowski, O. Festin, P. Svedlindh, M. Haase and H. Weller, *J. Am. Chem. Soc.*, 2003, **125**, 9090-9101.
14. E. V. Shevchenko, D. V. Talapin, A. L. Rogach, A. Kornowski, M. Haase and H. Weller, *J. Am. Chem. Soc.*, 2002, **124**, 11480-11485.
15. C. Sangregorio, M. Galeotti, U. Bardi and P. Baglioni, *Langmuir*, 1996, **12**, 5800-5802.
16. J. B. Nagy, *Colloids Surf.*, 1989, **35**, 201-220.
17. N. Toshima, M. Harada, T. Yonezawa, K. Kushihashi and K. Asakura, *J. Phys. Chem.*, 1991, **95**, 7448-7453.
18. G. Schmid, A. Lehnert, J. O. Malm and J. O. Bovin, *Angew. Chem. Int. Ed.*, 1991, **30**, 874-876.
19. M. T. Reetz, W. Helbig and S. A. Quaiser, *Chem. Mater.*, 1995, **7**, 2227-2228.
20. M. T. Reetz and S. A. Quaiser, *Angew. Chem. Int. Ed.*, 1995, **34**, 2240-2241.
21. E. Cottancin, J. Lerme, M. Gaudry, M. Pellarin, J. L. Vialle, M. Broyer, B. Prevel, M. Treilleux and P. Melinon, *Phys. Rev. B*, 2000, **62**, 5179-5185.
22. G. Mattei, C. Maurizio, P. Mazzoldi, F. D'Acapito, G. Battaglin, E. Cattaruza, C. D. J. Fernandez and C. Sada, *Phys. Rev. B*, 2005, **71**, 195418.
23. Y. Mizukoshi, T. Fujimoto, Y. Nagata, R. Oshima and Y. Maeda, *J. Phys. Chem. B*, 2000, **104**, 6028-6032.
24. A. Henglein, *Langmuir*, 2001, **17**, 2329-2333.
25. Z. Y. Zhang, T. M. Nenoff, J. Y. Huang, D. T. Berry and P. P. Provencio, *J. Phys. Chem. C*, 2009, **113**, 1155-1159.
26. A. Henglein and D. Meisel, *Langmuir*, 1998, **14**, 7392-7396.
27. T. Teranishi and M. Miyake, *Chem. Mater.*, 1999, **11**, 3414-3416.
28. S. U. Son, Y. Jang, J. Park, H. B. Na, H. M. Park, H. J. Yun, J. Lee and T. Hyeon, *J. Am. Chem. Soc.*, 2004, **126**, 5026-5027.

29. M. Gaudry, E. Cottancin, M. Pellarin, J. Lerme, L. Arnaud, J. R. Huntzinger, J. L. Vialle, M. Broyer, J. L. Rousset, M. Treilleux and P. Melinon, *Phys. Rev. B*, 2003, **67**, 155409.
30. E. Cottancin, M. Gaudry, M. Pellarin, J. Lerme, L. Arnaud, J. R. Huntzinger, J. L. Vialle, M. Treilleux, P. Melinon, J. L. Rousset and M. Broyer, *Eur. Phys. J. D*, 2003, **24**, 111-114.
31. H. Portales, L. Saviot, E. Duval, M. Gaudry, E. Cottancin, M. Pellarin, J. Lerme and M. Broyer, *Phys. Rev. B*, 2002, **65**, 165422.
32. D. Poondi and J. Singh, *J. Mater. Sci.*, 2000, **35**, 2467-2476.
33. D. Poondi, T. Dobbins and J. Singh, *J. Mater. Sci.*, 2000, **35**, 6237-6243.
34. A. Kumar, C. Damle and M. Sastry, *Appl. Phys. Lett.*, 2001, **79**, 3314-3316.
35. G. Rossi, A. Rapallo, C. Mottet, A. Fortunelli, F. Baletto and R. Ferrando, *Phys. Rev. Lett.*, 2004, **93**, 105503.
36. A. Rapallo, G. Rossi, R. Ferrando, A. Fortunelli, B. C. Curley, L. D. Lloyd, G. M. Tarbuck and R. L. Johnston, *J. Chem. Phys.*, 2005, **122**, 194308.
37. F. Baletto, C. Mottet, A. Rapallo, G. Rossi and R. Ferrando, *Surf. Sci.*, 2004, **566**, 192-196.
38. M. Harb, F. Rabilloud and D. Simon, *J. Phys. Chem. A*, 2007, **111**, 7726-7731.
39. M. Harb, F. Rabilloud and D. Simon, *Chem. Phys. Lett.*, 2007, **449**, 38-43.
40. F. Calvo, E. Cottancin and M. Broyer, *Phys. Rev. B*, 2008, **77**, 121406.
41. G. Kresse and J. Furthmuller, *Phys. Rev. B*, 1996, **54**, 11169-11186.
42. G. Kresse and J. Furthmuller, *Comput. Mater. Sci.*, 1996, **6**, 15-50.
43. J. P. Perdew, K. Burke and M. Ernzerhof, *Phys. Rev. Lett.*, 1996, **77**, 3865-3868.
44. R. Stumpf, *Surf. Sci.*, 2007, **601**, L115-L119.
45. J. A. Creighton and D. G. Eadon, *J. Chem. Soc. Faraday Trans.*, 1991, **87**, 3881-3891.
46. D. Ferrer, A. Torres-Castro, X. Gao, S. Sepulveda-Guzman, U. Ortiz-Mendez and M. Jose-Yacaman, *Nano Lett.*, 2007, **7**, 1701-1705.
47. I. Srnova-Sloufova, F. Lednicky, A. Gemperle and J. Gemperlova, *Langmuir*, 2000, **16**, 9928-9935.
48. I. Srnova-Sloufova, B. Vlckova, Z. Bastl and T. L. Hasslett, *Langmuir*, 2004, **20**, 3407-3415.
49. Z. Y. Li, J. Yuan, Y. Chen, R. E. Palmer and J. P. Wilcoxon, *Appl. Phys. Lett.*, 2005, **87**, 243103.
50. L. F. Valadares, F. D. C. Braganca, C. A. da Silva, C. A. P. Leite and F. Galembeck, *J. Coll. Inter. Sci.*, 2007, **309**, 140-148.
51. F. Hofer, W. Grogger, G. Kothleitner and P. Warbichler, *Ultramicroscopy*, 1997, **67**, 83-103.
52. A. Henglein, *J. Phys. Chem. B*, 2000, **104**, 6683-6685.
53. A. Henglein, *Ber. Bunsen-Ges. Phys. Chem.*, 1977, **81**, 556-561.
54. V. A. Spasov, T. H. Lee, J. P. Maberry and K. M. Ervin, *J. Chem. Phys.*, 1999, **110**, 5208-5217.
55. J. H. Larsen, J. T. Ranney, D. E. Starr, J. E. Musgrove and C. T. Campbell, *Phys. Rev. B*, 2001, **63**, 195410.
56. E. J. Hart, *Science*, 1964, **146**, 19-25.
57. H. A. Schwarz and R. W. Dodson, *J. Phys. Chem.*, 1989, **93**, 409-414.
58. A. Henglein, *J. Phys. Chem.*, 1980, **84**, 3461-3467.
59. B. G. Ershov, *Russ. Chem. Bull.*, 2000, **49**, 1715-1721.

60. M. Breitenkamp, A. Henglein and J. Lilie, *Ber. Bunsen-Ges. Phys. Chem.*, 1976, **80**, 973-979.
61. J. H. Baxendale and R. S. Dixon, *Z. Phys. Chem.*, 1964, **43**, 161-176.
62. K. Leung, S. B. Rempe and O. A. von Lilienfeld, *J. Chem. Phys.*, 2009, submitted.
63. A. G. Shenstone, *J. Res. Natl. Stand. A*, 1970, **74**, 801.
64. D. D. Wagman, W. H. Evans, V. B. Parker, R. H. Schumm, I. Halow, S. M. Bailey, K. L. Churney and R. L. Nuttall, *J. Phys. Chem. Ref. Data*, 1982, **11**, 1-392.
65. J. Turkevich, P. C. Stevenson and J. Hillier, *Discu. Faraday Soc.*, 1951, **11**, 55-75.
66. J. Turkevich, *Gold Bull.*, 1985, **18**, 86-91.
67. A. Henglein and M. Giersig, *J. Phys. Chem. B*, 1999, **103**, 9533-9539.
68. A. Henglein, *J. Phys. Chem.*, 1979, **83**, 2209-2216.
69. M. Kelm, J. Lilie, A. Henglein and E. Janata, *J. Phys. Chem.*, 1974, **78**, 882-887.
70. A. Henglein, *Langmuir*, 1999, **15**, 6738-6744.
71. M. Treguer, C. de Cointet, H. Remita, J. Khatouri, M. Mostafavi, J. Amblard, J. Belloni and R. de Keyzer, *J. Phys. Chem. B*, 1998, **102**, 4310-4321.
72. J. Belloni, M. Mostafavi, H. Remita, J. L. Marignier and M. O. Delcourt, *New J. Chem.*, 1998, **22**, 1239-1255.
73. Nanostructured Mat. 1999, 12, 987; Robinson, etal., SAND2009-0218P

DISTRIBUTION

1	MS-0899	Technical Library, 9536 (electronic copy)
1	MS-0123	D. Chavez, LDRD Office, 1011 (electronic copy)
1	MS-1415	Tina Nenoff, 1114 (electronic copy)
1	MS-1415	Kevin Leung, 1114 (electronic copy)
1	MS-1415	Roland Stumpf, 1114 (electronic copy)
1	MS-1415	Carlos Gutierrez, 1114 (electronic copy)
1	MS-1314	Jianyu Huang, 1132 (electronic copy)
1	MS-1315	Sean Hearne, 1132 (electronic copy)
1	MS-1411	Ping Lu, 1822 (electronic copy)
1	MS-886	Jim Aubert, 1822 (electronic copy)
1	MS-1303	Paula Provencio, 1111 (electronic copy)
1	MS-1056	Barney Doyle, 1111 (electronic copy)

1	Zhenuan Zhang, Duke University, zz27@duke.edu (electronic copy)
1	Donald Berry, Retired, thelranger@yahoo.com (electronic copy)

Sandia National Laboratories